CFD Simulations of the IHF Arc-Jet Flow: Compression-Pad/Separation Bolt Wedge Tests

Tahir Gökçen* and Kristina A. Skokova†
AMA Inc., NASA Ames Research Center, Moffett Field, CA 94035

This paper reports computational analyses in support of two wedge tests in a high enthalpy arc-jet facility at NASA Ames Research Center. These tests were conducted using two different wedge models, each placed in a free jet downstream of a corresponding different conical nozzle in the Ames 60-MW Interaction Heating Facility. Each panel test article included a metallic separation bolt imbedded in Orion compression-pad and heatshield materials, resulting in a circular protuberance over a flat plate. The protuberances produce complex model flowfields, containing shock-shock and shock-boundary layer interactions, and multiple augmented heating regions on the test plate. As part of the test calibration runs, surface pressure and heat flux measurements on water-cooled calibration plates integrated with the wedge models were also obtained. Surface heating distributions on the test articles as well as arc-jet test environment parameters for each test configuration are obtained through computational fluid dynamics simulations, consistent with the facility and calibration measurements. The present analysis comprises simulations of the nonequilibrium flowfield in the facility nozzle, test box, and flowfield over test articles, and comparisons with the measured calibration data.

Nomenclature

c_i	=	species mass fraction for species *i*
D_e	=	nozzle exit diameter, cm (or in)
D_{bolt}	=	outer diameter of the circular protrusion on the test plate, cm
h	=	enthalpy, MJ/kg
h_o	=	total enthalpy, MJ/kg
h_{ob}	=	mass-averaged total enthalpy (or bulk enthalpy), MJ/kg
h_{ocl}	=	centerline total enthalpy, MJ/kg
h_{step}	=	total step height of the circular protrusion, cm
h_{step1}	=	height of the first step of the circular protrusion, cm
I	=	arc current, A
M	=	Mach number
M_e	=	boundary-layer edge Mach number
$\dot{m}$	=	mass flow rate, g/s
p	=	pressure, kPa
p_{box}	=	test box pressure, torr
p_{ch}	=	arc-heater pressure, kPa
p_o	=	total pressure, kPa
p_1, p_2, p_3	=	pressure gages on the wedge calibration plate, kPa
p_s	=	surface pressure, kPa
p_{t2}	=	pitot pressure or model stagnation pressure, kPa
q_s	=	surface heat flux, W/cm^2
q_{CWFC}	=	cold-wall full-catalytic heat flux, W/cm^2
q_{HWFC}	=	hot-wall full-catalytic heat flux, W/cm^2
Q_1-Q_6	=	heat flux gages on the wedge calibration plate (Q_1-Q_4 on centerline), W/cm^2

* Senior Research Scientist, MS 230-2, Associate Fellow AIAA
† Senior Research Scientist, MS 234-1

Re_x = Reynolds number based on the running length from the wedge nose, $\rho_e u_e s/\mu_e$
r_c = model corner radius, cm
r_n = nose radius, cm
s = arc-length coordinate, m
T = temperature or translational-rotational temperature, K
T_v = vibrational-electronic temperature, K
u = axial velocity component, m/s
V = arc voltage, V
x_{ml} = model location from the nozzle exit plane, cm
δ = boundary layer thickness based on total enthalpy profile, cm
ε = hemispherical emissivity, 0.89
ρ = density, kg/m^3
ρ_e = density at the boundary-layer edge, kg/m^3
μ_e = viscosity at the boundary-layer edge, Pa.s
τ_s = surface shear, Pa

I. Introduction

Arc-jet facilities provide the primary means to study the performance of various types of thermal protection systems (TPS) used on the outer surfaces of spacecraft in an aerothermodynamic heating environment. In a high enthalpy arc-jet facility, a test gas, usually air or a mixture of nitrogen, oxygen and argon, is passed through an electric arc discharge where the energy is added to the flow. The test gas is then expanded through a converging-diverging nozzle into an evacuated test chamber to produce high-enthalpy supersonic or hypersonic flow. NASA Ames Research Center (ARC) has four arc-jet facilities within its Arc-Jet Complex.[1]

Since Avcoat, the thermal protection system used on the Orion and Apollo spacecraft, does not have the mechanical strength to support the mechanical loads between the crew module and service module during launch, densified compression-pads are used to support these loads. As a result of one compression-pad design, circular recessed cavities or protuberances are embedded in the heatshield. [2-3] These cavities or protuberances disturb the flow during atmospheric reentry, producing augmented heating regions locally and downstream. A related compression-pad system design results in a protuberance on the compression-pad material and heatshield. The present arc-jet tests are conducted in the NASA Ames 60-MW Interaction Heating Facility (IHF) to evaluate such a compression-pad design and to investigate effects of the melting metallic separation bolt used in the design on performance of the compression-pad and heatshield materials. Two separate tests, employing two different blunted wedge holders, were conducted in the IHF conical nozzles. Each panel test article included a metallic separation bolt or a circular protuberance. Due to these protuberances, model flowfields include many complex flow features such as shock-shock and shock-boundary layer interactions, resulting in multiple augmented heating regions on the test plate. In order to characterize the aerothermodynamic heating environment over the test articles, calibration plates with an array of heat flux calorimeter and pressure gages are also used. These IHF wedge tests provide a sub-scale testing capability for the Orion compression-pad designs. Since the arc-jet flowfield over the compression-pad separation-bolt test article is complex, traceability of the arc-jet test environment to the flight environment can only be achieved through validated computational tools. In fact, for the test articles with the separation bolt, computational fluid dynamics (CFD) simulation is the only viable option to provide surface heating and pressure distributions.

In support of these arc-jet wedge tests, CFD simulations are used: (1) to characterize the arc-jet test environment and its parameters consistent with the facility and calibration measurements; and (2) to provide surface quantities (pressure, heat flux and shear distributions) for material thermal response and thermal stress analyses, and estimates of other test environment parameters of interest such as boundary layer thickness and edge Mach number. The primary objective of the paper is to report these CFD simulations. The present analysis comprises computational Navier-Stokes simulations of the nonequilibrium flowfield in the facility nozzle and test box as well as the flowfield over the models, and comparisons with the experimental measurements.

II. Arc-Jet Facility and Tests

The IHF at NASA ARC consists of a constricted arc heater, a 60-MW DC power supply, interchangeable conical and semi-elliptical nozzles, a test chamber, and supplementary systems including steam ejector vacuum system, cooling-water system and data acquisition system. The IHF is designed to operate with a set of conical nozzles or a semi-elliptical nozzle at total pressures of 1-9 atm and total bulk enthalpies of 2-28 MJ/kg (air).[4] The 60-MW constricted arc heater produces high-temperature test gas for both nozzles. The conical nozzle configurations of the IHF are suitable for tests of stagnation coupon and blunted wedge models in hypersonic flow, while the semi-elliptical nozzle configuration is designed mainly for testing flat panels in hypersonic boundary-layer heating environments. Figure 1 shows a schematic diagram of the IHF with its interchangeable nozzles and a photograph of a wedge test.

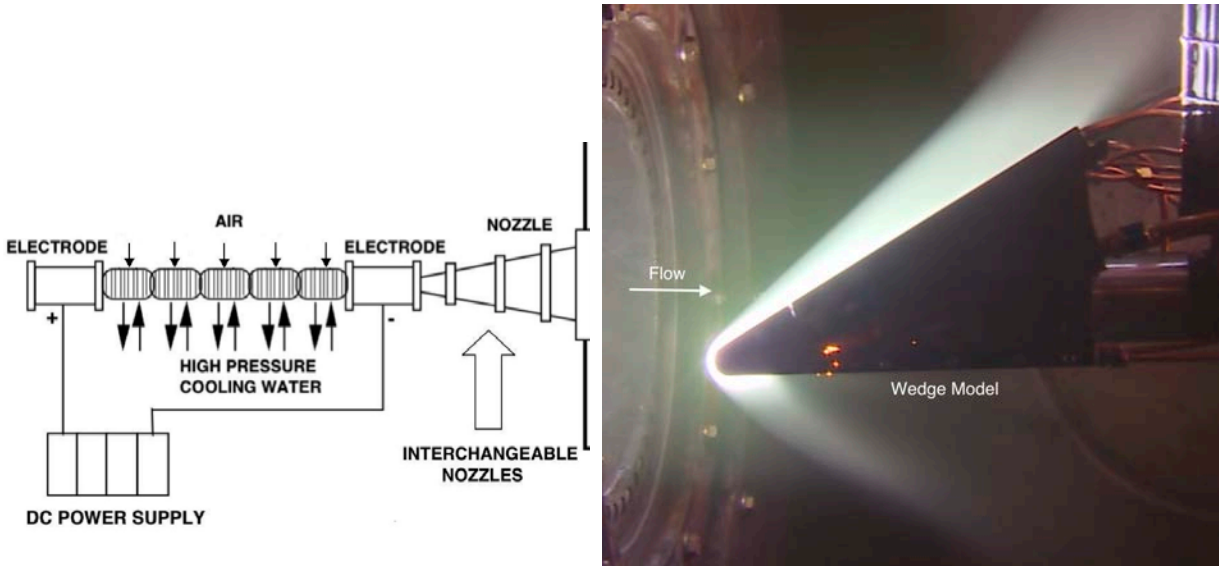

(a) IHF arc-heater/nozzles sketch **(b) Wedge model in a conical nozzle test**

Figure 1. IHF sketch and a photograph of a conical nozzle/wedge test.

For the present paper, computational analyses of the two wedge tests conducted using two different IHF nozzles are considered. The first one is the IHF 6-inch conical nozzle tests using a 7-inch wide wedge holder, and the second one is the IHF 13-inch conical nozzle tests using a larger 9.2-inch wide wedge holder. Both IHF 6-inch and 13-inch nozzles have the same throat diameter of 6.033 cm (2.375 in) and the same 10° half-angle for the diverging section, while their exit diameters are 15.24 cm (6 in) and 33.02 cm (13 in), respectively. Note that the IHF 6-inch nozzle also includes a 40° extension piece (4.6 cm long) attached to the nozzle exit. The 7-inch wedge holder was originally designed by H. Moody of Thermal Technologies Inc. (TTI),[5] and the 9.2-inch wedge was designed by D. Driver of NASA ARC.[6] The smaller wedge has a 20° half-angle, a nose radius of 0.9525 cm, and a width of 17.78 cm, while the larger wedge model has a 30° half-angle, a nose radius of 1.27 cm, and 23.37 cm width. Both wedge models are made of copper and water-cooled, and they can accommodate either a calibration plate or a TPS sample plate for testing. Both calibration plates are instrumented with 6 Gardon gage calorimeters and 3 pressure transducers. Figure 2 shows photographs of the two wedge models, each mounted with a calibration plate and a test article. Test articles used include one or two TPS panels and an imbedded bolt (or a circular protuberance) with different diameters and heights.

In the IHF 6-inch nozzle/7-inch wedge tests (IHF 309 test series), effects of the melting metallic separation bolt on performance of the compression-pad material (3DMAT, woven TPS) are investigated, while in the IHF 13-inch nozzle/9.2-inch wedge tests (IHF 305 test series), effects of the melting bolt on performance of both compression-pad and heatshield (molded Avcoat) materials downstream are investigated. For both tests, each panel test article consists of a circular protrusion on the plate, representing a sub-scale metallic bolt resulting from the compression-pad system design. Each circular protrusion is formed by combination of two different steps: the first step with the

height of h_{step1} starts at the outer bolt diameter, perpendicular to the plate, while the second step starts at the top of the first step with a bevel angle of 45° and reaches the total step height of h_{bolt} at a smaller diameter at the bolt top. For the 7-inch wedge, an outer bolt diameter of D_{bolt} = 5.156 cm (2.03 in) and step heights of h_{bolt} = 0.381 cm (0.15 in) and h_{step1} = 0.127 cm (0.05 in) are used, and the distance from the test plate leading edge to the bolt leading edge is 2.54 cm (1 in). For the 9.2-inch wedge, an outer bolt diameter of D_{bolt} = 4.128 cm (1.625 in) and step heights of h_{bolt} = 1.016 cm (0.4 in) and h_{step1} = 0.537 cm (0.2115 in) are used, and the distance from the test plate leading edge to the bolt leading edge is 1.27 cm (0.5 in). For the IHF 6-inch nozzle tests, the 7-inch wedge models were tested at 10.16 cm (4 in) downstream of the nozzle exit and placed on centerline. For the IHF 13-inch nozzle tests, the 9.2-inch wedge models were also tested at 10.16 cm downstream of the nozzle exit but the wedge leading edge was placed 3.81 cm (1.5 in) below the nozzle centerline.

(a) 7-in wedge model, calibration plate

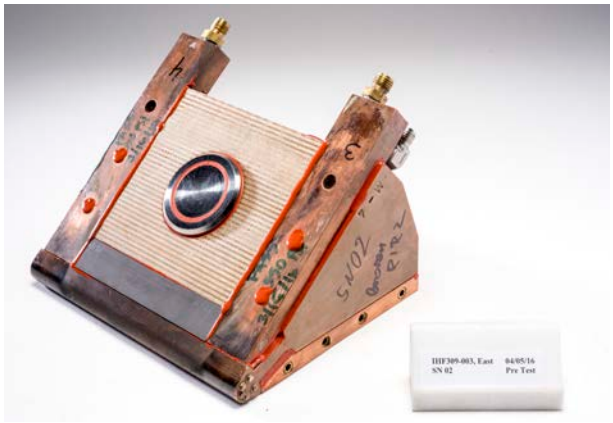

(b) 7-in wedge model, test article

(c) 9.2-in wedge model, calibration plate

(d) 9.2-in wedge model, test article

Figure 2. Photographs of two wedge models.

III. Computational Approach

Computational analyses of arc-jet tests are performed through simulation of nonequilibrium expanding flow in the arc-jet nozzle and supersonic jet, and simulation of the flow in the test box and around the test articles. For all CFD calculations, the Data Parallel Line Relaxation (DPLR) code,[7,8] a NASA Ames in-house flow solver, is used. DPLR has been employed extensively at Ames for hypersonic flight, planetary entry and arc-jet simulations. DPLR provides various options for thermophysical models and formulation. For CFD calculations presented in this paper, two-dimensional axisymmetric or three-dimensional Navier-Stokes equations, supplemented with the equations accounting for nonequilibrium kinetic processes, are used in the formulation. The thermochemical model employed for the arc-jet flow includes six species (N_2 O_2, NO, N, O, Ar), and the thermal state of the gas is described by two temperatures (translational-rotational and vibrational-electronic) within the framework of Park's two-temperature model.[9]

The flowfield in an arc-jet facility, from the arc heater to the test section, is a very complex, three-dimensional flow with various nonequilibrium processes occurring. In order to simulate the flowfield, several simplifying assumptions are made, and corresponding numerical boundary conditions are prescribed for CFD simulations. The present computational approach follows our earlier work for the IHF and other arc-jet facilities,[10-13] and is described briefly here.

Simulations of the arc-jet facility flow are started from the nozzle inlet. The total enthalpy and its radial profile at the inlet are prescribed based on the facility and calibration data, and the flow properties at the inlet are assumed to be in thermochemical equilibrium. Measured facility data, namely, the total pressure, mass flow rate, and test box pressure, are used as boundary conditions. The calibration data obtained include stagnation calorimeter heat flux and pressure in the freestream, and pressure and heat flux measurements on the water-cooled wedge calibration plates. All metallic surfaces, water-cooled nozzle walls, and calorimeter model and calibration plate surfaces (copper slug or Gardon gages), are assumed to be fully catalytic to recombination reactions of atomic oxygen and nitrogen at a constant temperature of 500 K, while the un-cooled test plate temperatures are computed using a radiative equilibrium surface boundary condition ($\varepsilon = 0.89$). The test box is included in CFD simulations, primarily to account for the free jet expansion formed by the under-expanded flow exiting the nozzle to the test box and its potential effects on model flowfields. The jet expansion within the test box is primarily determined by the test box static pressure, which is one of the facility measurements and is prescribed as a boundary condition.

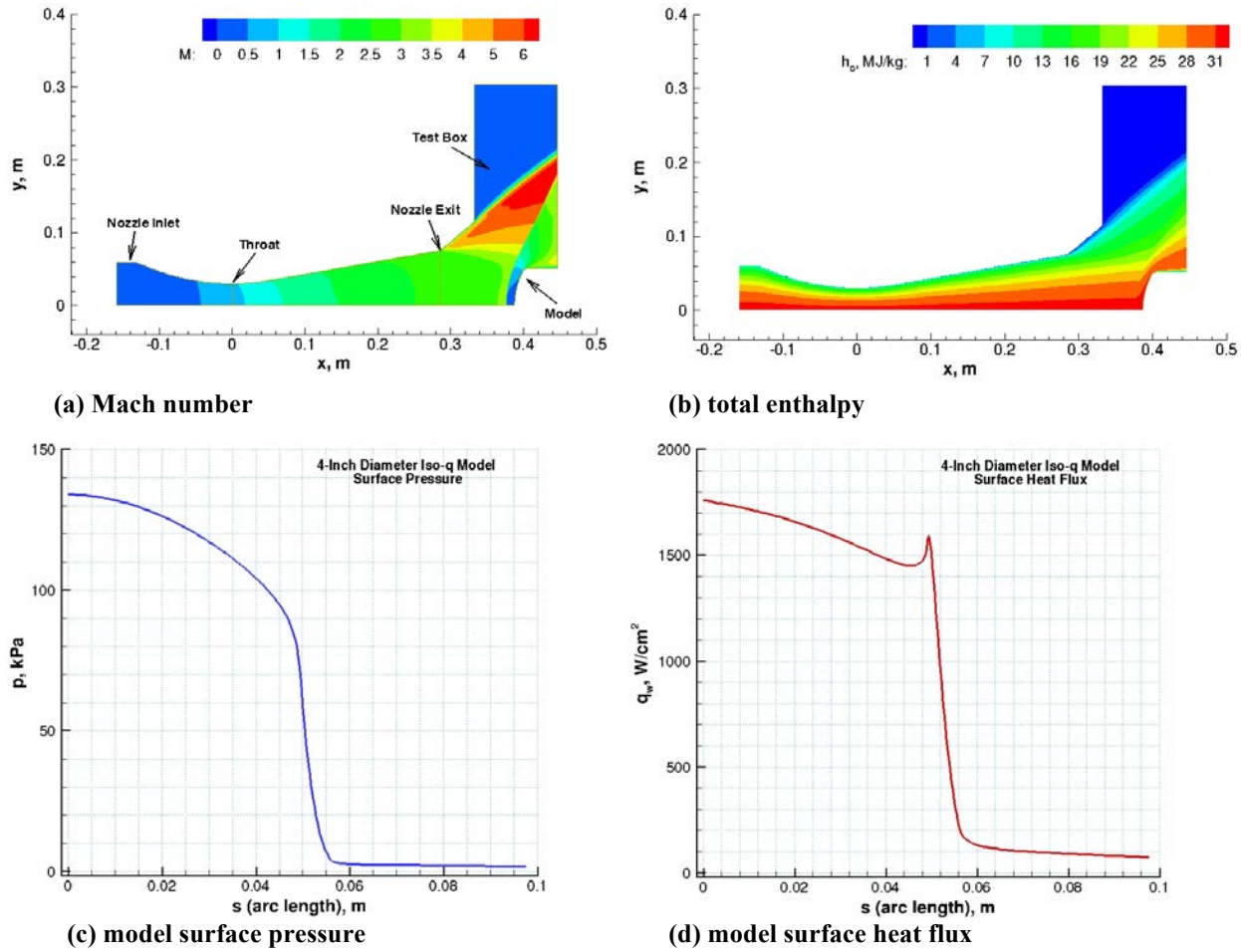

(a) Mach number **(b) total enthalpy**

(c) model surface pressure **(d) model surface heat flux**

Figure 3. Computed IHF 6-inch nozzle flowfield including the test box and a 10.16-cm diameter iso-q calorimeter model: $\dot{m}$ = 849 g/s, h_{ob} = 20.9 MJ/kg, h_{ocl} = 31.7 MJ/kg, parabolic enthalpy profile, 6.4% Ar, p_{box} = 2 torr. Calorimeter data (IHF 309 Runs 1-1 and 2-1): 1759 W/cm^2 and 134 kPa.

IV. Presentation of Results

A. Stagnation calorimeter model simulations

Stagnation calorimeter models are used to calibrate the test conditions, and to infer the centerline total enthalpy of the arc-jet flow. The primary objective of the stagnation model calculations is to estimate the centerline total enthalpy of the arc-jet flow consistent with the facility and calorimeter measurements. As an illustration of a typical axisymmetric simulation, Fig. 3 shows a computed IHF 6-inch nozzle flowfield including the test box and a stagnation calorimeter model, including the corresponding computed model surface quantities for this case.

At the nozzle inlet, uniform pressure and a non-uniform parabolic enthalpy profile are specified such that the centerline calorimeter data are reproduced with the computations. It is important to reproduce both measured surface pressure and heat flux with CFD simulations in order to estimate the centerline total enthalpy. Note that the estimation of centerline total enthalpy from CFD simulations this way is analogous to the ASTM standard E637-05,[14] except that the calorimeter surface heat flux and pressure are predicted by CFD simulations, replacing the heat transfer theory used in the standard.

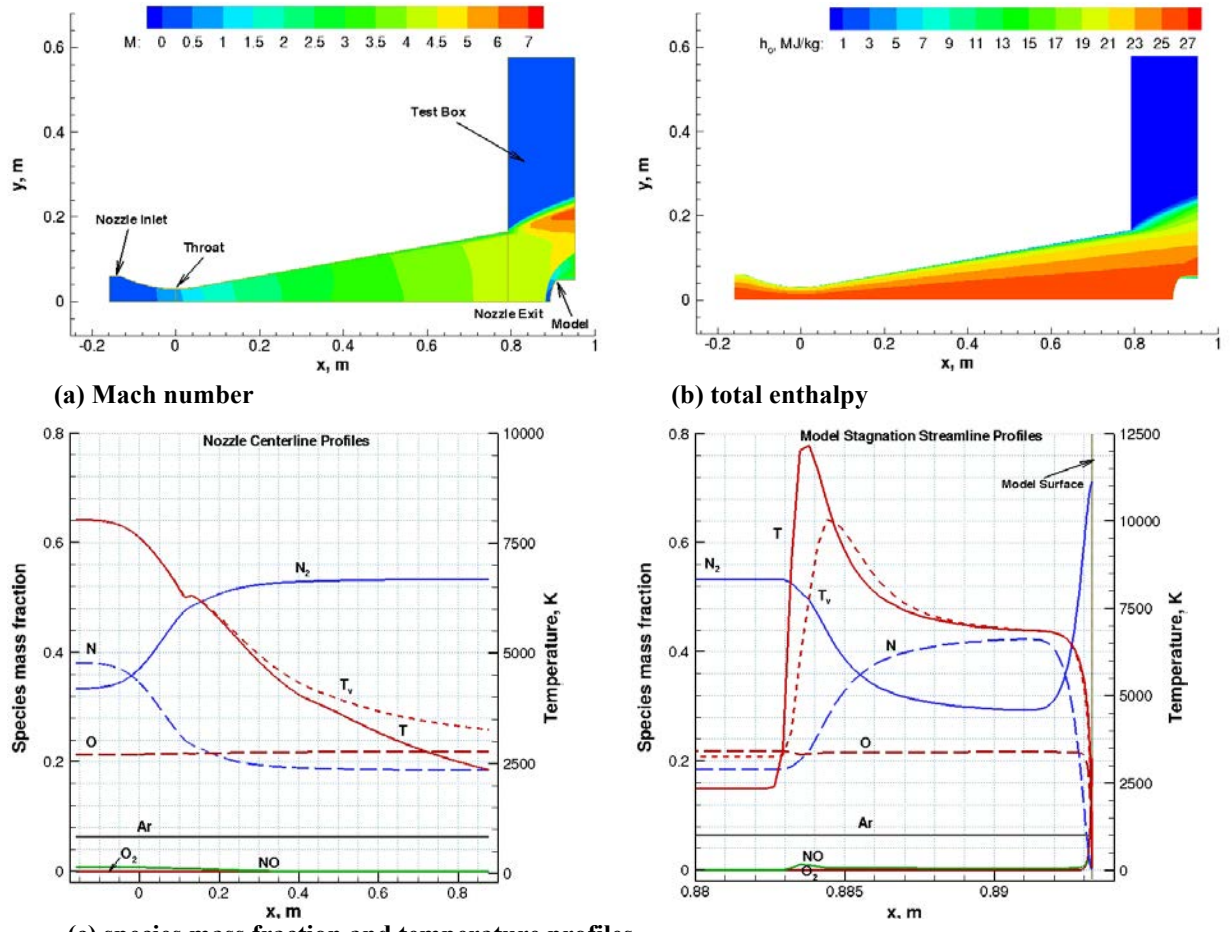

(a) Mach number **(b) total enthalpy**

(c) species mass fraction and temperature profiles

Figure 4. Computed IHF 13-inch nozzle flowfield including the test box and a 10.16-cm diameter iso-q calorimeter model: $\dot{m}$ = 849 g/s, h_{ob} = 22.8 MJ/kg, h_{ocl} = 26.7 MJ/kg, parabolic enthalpy profile, 6.4% Ar, p_{box} = 2 torr. Corresponding calorimeter data (IHF 305 Runs 3-1 and 4-1): 818 W/cm^2 and 41.8 kPa.

As described earlier, each wedge test included measurements of heat flux and pressure on a water-cooled calibration plate. The CFD-estimated centerline enthalpies inferred from the stagnation calorimeter data are further refined to best reproduce both calorimeter and calibration plate data, provided that these adjustments are within the facility data constraints and their measurement uncertainties. Since CFD simulations for the wedge flowfields

provide estimates of various surface and flow quantities of interest such as surface shear, boundary layer thickness and boundary layer edge Mach number, the reliability of these estimates depends on how well the CFD simulations reproduce the measured quantities.

In order to provide some insight into the arc-jet flowfield chemistry within these nozzles, another example from IHF 13-inch nozzle/calorimeter model simulations is shown in Fig. 4. Because of the nonequilibrium expansion process in arc-jet nozzles, the chemical composition freezes near the throat where the flow is dissociated and vibrationally excited. As shown in Fig. 4c, for this case, the computations predict that the flow is chemically frozen but remains in vibrational nonequilibrium before it reaches the nozzle exit. Note that oxygen remains fully dissociated within the entire flowfield except in the boundary layer near the walls, while nitrogen is partially dissociated.

B. IHF 6-inch nozzle flow/20° wedge model simulations

First, CFD flowfield simulations for the wedge model with the calibration plate configuration are presented, including comparisons with the calibration data. CFD simulations of the test article with the circular bolt protrusion follow.

Simulations of the 20° wedge model with the calibration plate

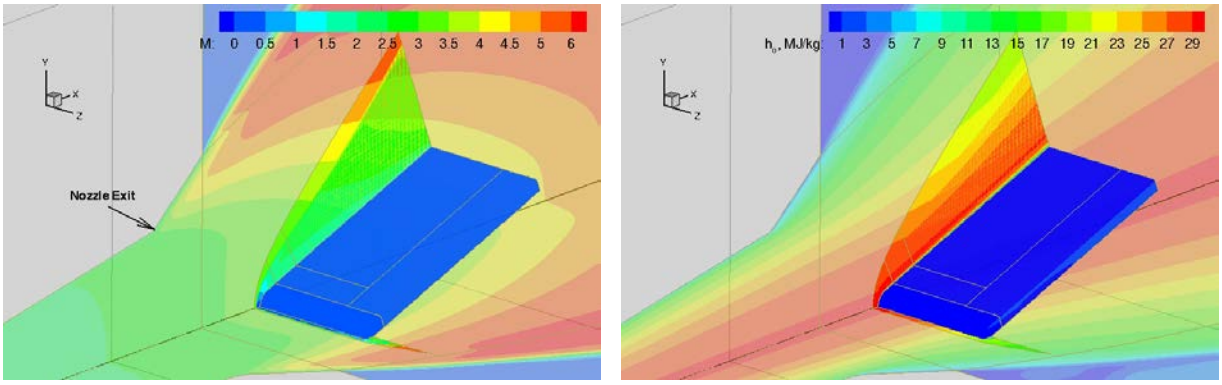

a) Mach number **(b) total enthalpy**

Figure 5. Computed flowfield contours of the IHF 6-inch nozzle flow and test box with the 20° wedge model: $\dot{m}$ = 849 g/s, h_{ob} = 21.5 MJ/kg, h_{ocl} = 29.2 MJ/kg, parabolic enthalpy profile, 6.4% Ar, p_{box} = 2 torr.

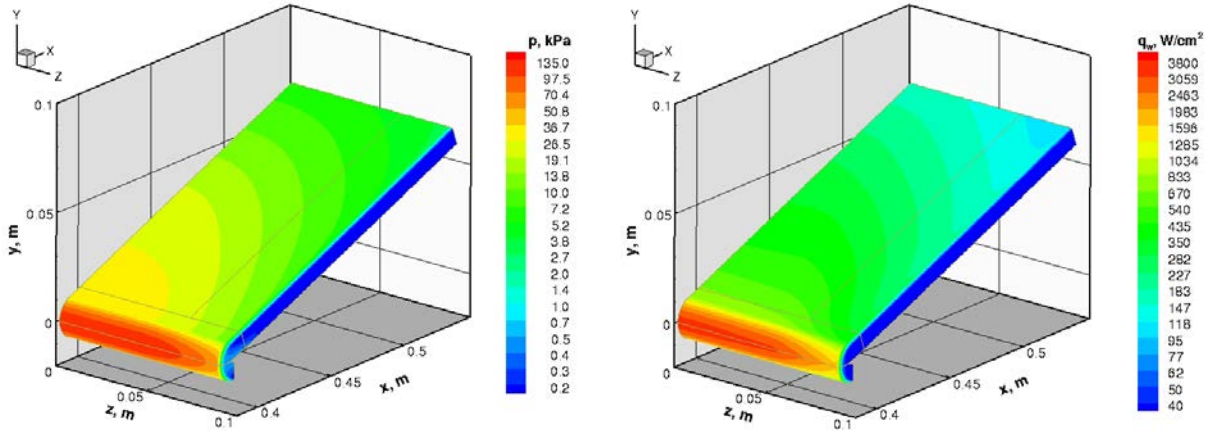

(a) pressure **(b) heat flux**

Figure 6. Computed surface quantities of the 20° wedge model with the water-cooled calibration plate. IHF 6-inch nozzle flow: $\dot{m}$ = 849 g/s, h_{ob} = 21.5 MJ/kg, h_{ocl} = 29.2 MJ/kg, 6.4% Ar.

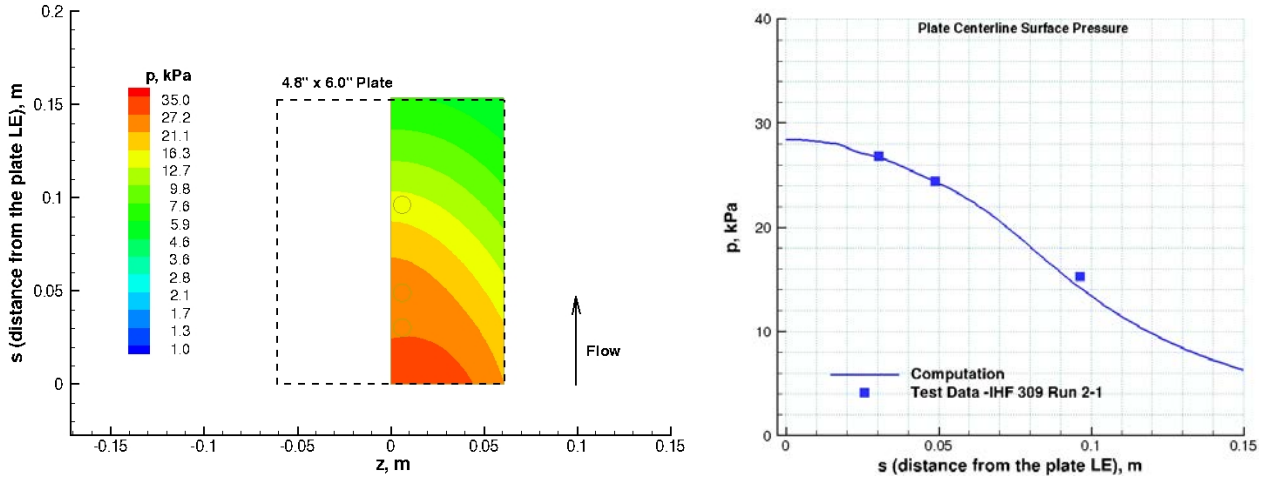

(a) pressure

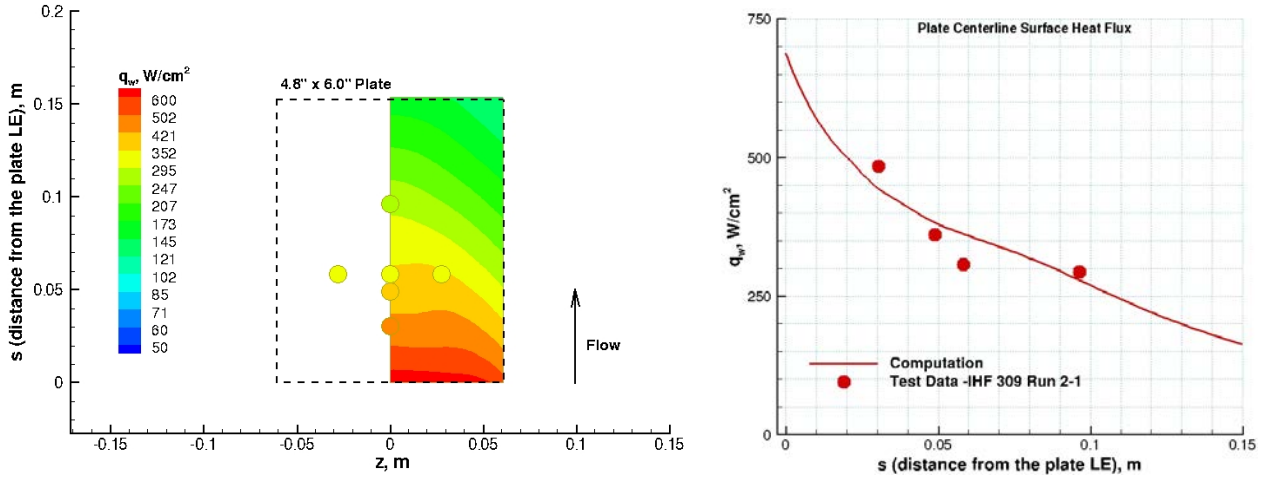

(b) heat flux

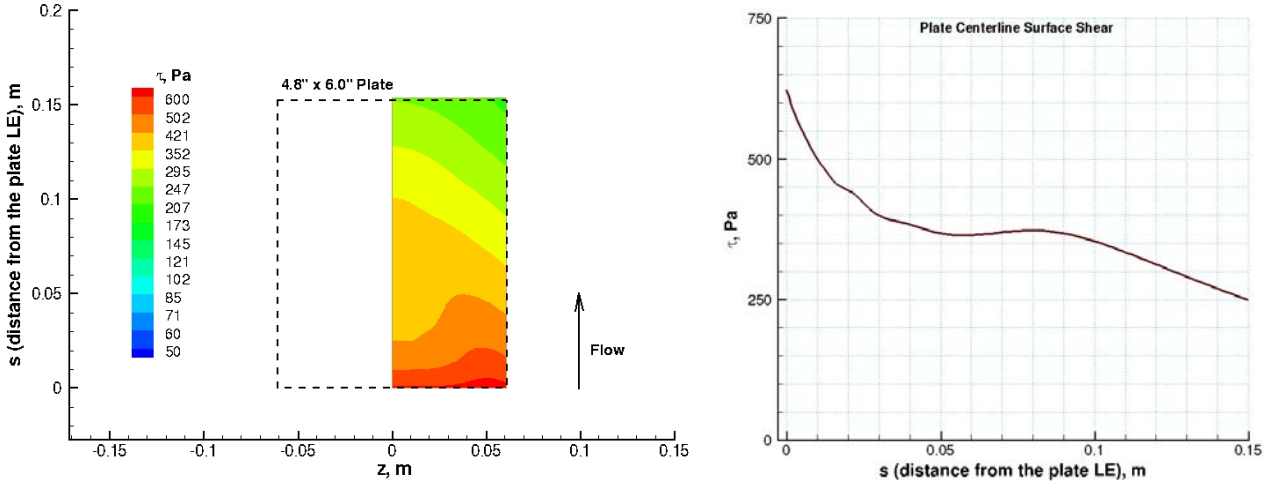

(c) shear

Figure 7. Computed surface quantities of the calibration plate using the 20° wedge model and comparisons with the calibration data. IHF 6-inch nozzle flow: $\dot{m}$ = 849 g/s, h_{ob} = 21.5 MJ/kg, h_{ocl} = 29.2 MJ/kg, 6.4% Ar. Symbols color-coded with the contour colors are the test data from IHF 309 Run 2-1.

Figure 5 shows the computed Mach number and total enthalpy contours of the IHF 6-inch nozzle and test box flow. The contours are shown on the x-y and x-z symmetry planes of the flowfield near the nozzle exit and on other planes of interest for the flowfield of the test box and over the wedge model. The expansion waves emanating from the nozzle lip at the exit to the test box are clearly seen in the Mach number contours. These waves ordinarily affect the shape and strength of the shock formed over the wedge model, thus affecting the pressure and heat flux distributions on the model.

Figure 6 shows contours of the computed surface quantities (pressure and heat flux) of the wedge model with the calibration plate. Note that the surface pressure drops significantly along the wedge centerline. The pressure drop observed along the plate centerline is primarily due to the following two factors: three-dimensional conical flow expansion over the side of the model (cross flow effects), and interaction of the expansion waves from the nozzle exit with the bow shock wave of the wedge model. As expected, the effect of the expansion wave becomes increasingly important when the model size and the nozzle exit diameter are comparable.

Table 1. Summary of facility conditions, stagnation calorimeter and 20° wedge calibration plate data obtained in the IHF 6-inch nozzle at x_{ml} = 10.16 cm, and corresponding CFD estimated parameters.

	IHF 309 Tests Facility/Calibration Data		
	Run 1-1	**Run 2-1**	**Run 3-1**
p_{ch}, kPa	826	829	819
I, A	5985	5993	5988
V, V	6762	6776	6713
$\dot{m}$, g/s	849	849	849
$c_{Ar,\,\%}$	6.4	6.4	6.4
$h_{ob}\,(W)$, MJ/kg	21.5	21.7	21.0
p_1, p_2, p_3, kPa	26.1, 23.6, 14.4	26.8, 24.4, 15.3	25.9, 23.5, 14.2
Q_5, W/cm^2	330	334	297
Q_1, Q_2, Q_3, Q_4, W/cm^2	472, 356, 301, 285	485, 361, 307, 294	515, 365, 313, 297
Q_6, W/cm^2	344	350	364
q_{isoq}, W/cm^2	1744	1773	N/A
p_{isoq}, kPa	133.9	134.1	N/A
	CFD Estimates		
$\dot{m}$, g/s	849		
$c_{Ar,\,\%}$	6.4		
h_{ob}, MJ/kg	21.5		
$h_{ocl,}$ MJ/kg	29.2		
p_s, kPa	27.6 – 9.5		
q_s (CWFC), W/cm^2	499 – 216		
q_s (HWFC), W/cm^2	417 – 203		
τ_s, Pa	443 – 308		
δ, cm	0.25		
M_e	1.56		
Re_x	8.1x10^3		

Note that CFD-estimated surface quantities are given as a range from the test plate leading edge to 10.2 cm downstream along the symmetry plane, and estimates for δ and M_e are given at the test plate leading edge location. The facility bulk enthalpy estimates, $h_{ob}\,(W)$, are determined by the equilibrium sonic flow method of Winovich.[15]

Figure 7 shows computed calibration-plate surface quantities and comparisons with the measured calibration plate data. The contour plots show computed surface pressure and heat flux on one half of the calibration plate, and the symbols in the contour plots are the measurements, color coded with the same contour levels. A complete uncertainty analysis of the calibration plate measurements is not available. However, based on empirical evidence (historical Ames arc-jet data with similar measurements), the heat flux measurements are estimated to be accurate to within ±15% and the pressure measurements to within ±5%. Note that computed and measured surface pressure values are in good agreement. The agreement in the rate of pressure drop along the plate centerline indicates that wave interaction and three dimensional effects are adequately captured by the computations.

Table 1 gives a summary of the facility and calibration data obtained in IHF 309 tests, and corresponding CFD estimates. The tabulated values of surface pressure, heat flux (CWFC and HWFC), and shear are given for the test plate centerline (not for the calibration plate). The wedge model in the test plate configuration includes a graphite conditioning plate (~2.0 cm or 0.8 in). Note that CFD simulations of the wedge model with the smooth test plate for HWFC heat flux estimates are not presented; only the results are reported in Table 1. The hot-wall fully-catalytic heat flux predictions are important for flight to arc-jet test traceability purposes since the flight environment definition is usually based on these quantities.

Simulations of the 20° wedge model with the test plate

Once arc-jet test flow conditions are characterized with CFD simulations, consistent with the facility and calorimeter/calibration data, CFD simulations of the wedge model wih the test article are performed.

Figure 8 shows the geometry of the 20° wedge model with the test plate and computed surface temperature contours. The water-cooled copper sections of the model are assumed to be at 500 K while the test plate temperatures are computed using a radiative equilibrium boundary condition. Note that there is a graphite conditioning plate in the wedge holder installed upstream of the test plate (~2 cm in length) as shown in Fig. 8a. In other words, the leading edge of the test plate with the compression-pad material and metallic bolt is about 2 cm downstream of the calibration plate leading edge shown in Fig 7.

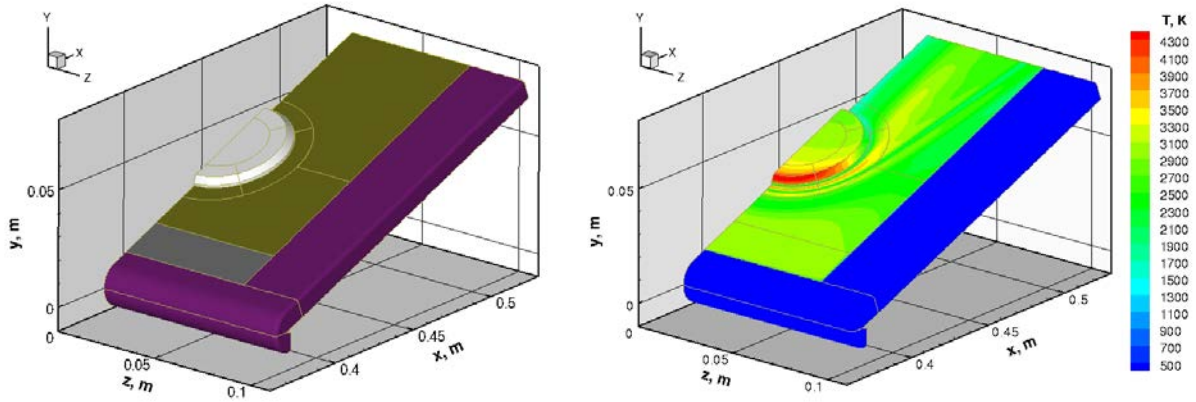

(a) 20° wedge model geometry **(b) surface temperature**

Figure 8. Geometry of the 20° wedge model with the test plate and computed surface temperature contours. IHF 6-inch nozzle flow: $\dot{m}$ = 849 g/s, h_{ob} = 21.5 MJ/kg, h_{ocl} = 29.2 MJ/kg, 6.4% Ar.

Figure 9 shows contours of the computed surface pressure, heat flux and shear stress on one half of the test plate with the bolt and the corresponding profiles along the plate centerline. In order to make interpretation of the centerline profiles easier, the geometry of the test plate is also shown. Note that the flow around the bolt is complex and three-dimensional. Due to the bolt protrusion, flowfield upstream of the bolt is separated, and two shock waves are formed. CFD simulations predict that a separation bubble is formed at the leading of the bolt. The first shock wave originates at the upstream edge of this bubble. As a result of shock-wave boundary layer interaction, the flow separation region extends upstream, and another shock wave is formed at the reattachment point. Two primary augmented heating regions upstream of the bolt and around the bolt are predicted by CFD simulations. Details of the flowfield features near the bolt will also be discussed later in the paper. The heat flux contours in Fig. 9b clearly show these two augmented heating regions around the bolt. The computed surface shear stress contours are also

shown in Fig. 9c. These contours provide additional information about stagnant and separated regions in the flowfield, as these regions exhibit relatively low shear levels (e.g., both upstream and downstream of the bolt).

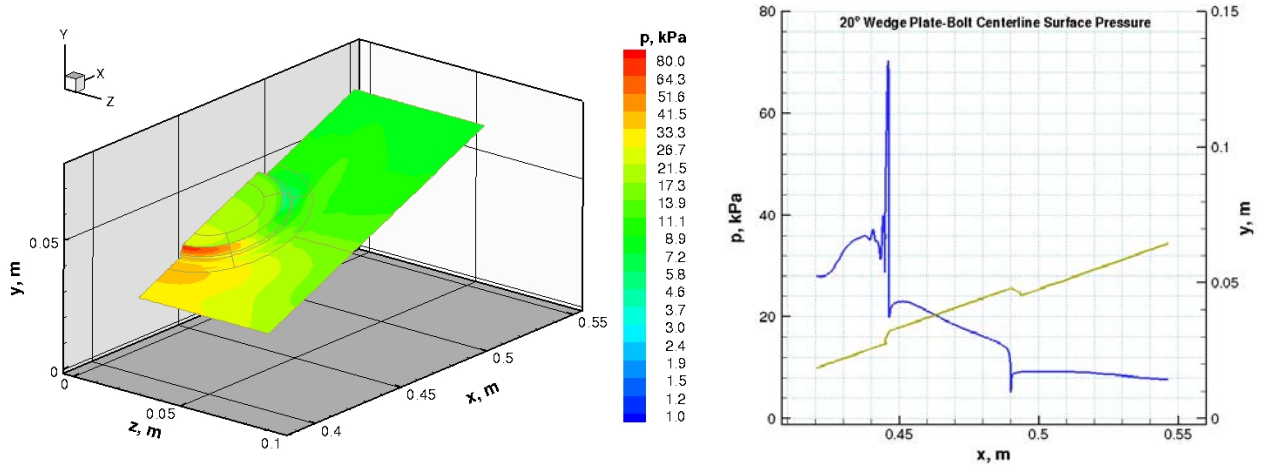

(a) pressure

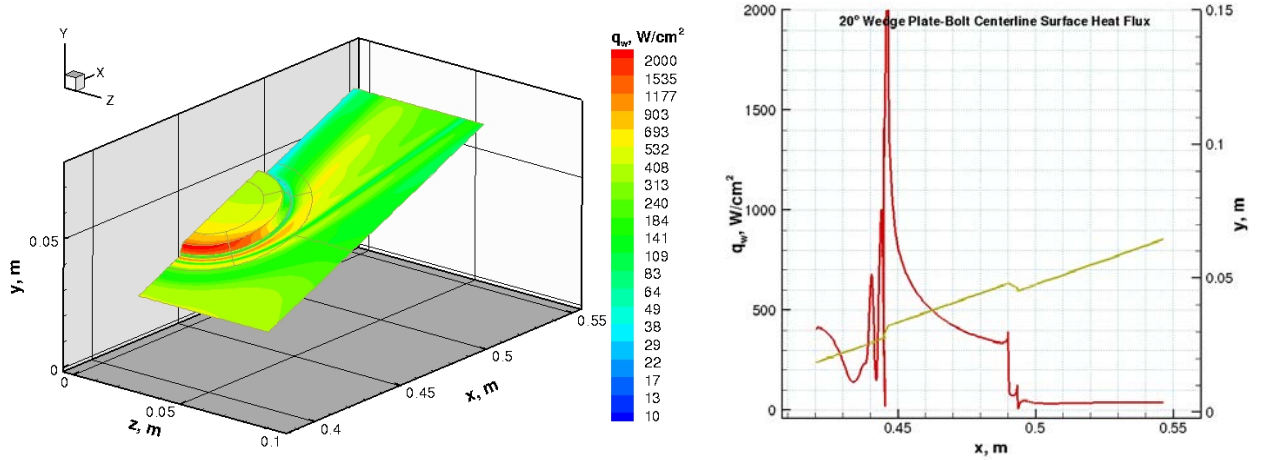

(b) heat flux

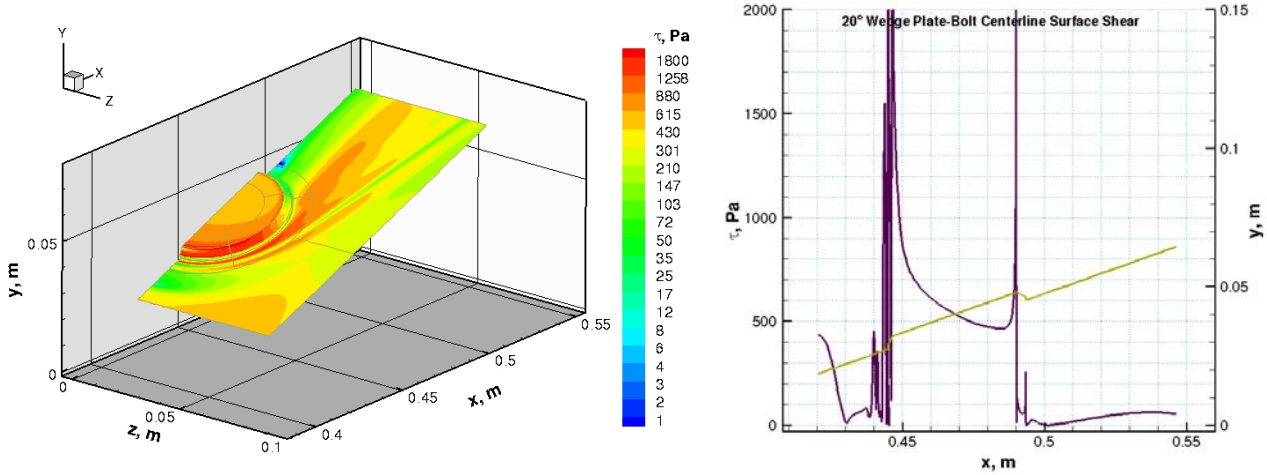

(c) shear

Figure 9. Computed surface quantities of the test plate using the 20° wedge model. IHF 6-inch nozzle flow: $\dot{m}$ = 849 g/s, h_{ob} = 21.5 MJ/kg, h_{ocl} = 29.2 MJ/kg, 6.4% Ar.

C. IHF 13-inch nozzle flow/30° wedge model simulations

Similar to the simulations presented for the IHF 6-inch nozzle tests, CFD flowfield simulations for the 30° wedge model with the calibration plate configuration are presented first. Then, CFD simulations of the wedge model with the test article including the circular bolt follow.

Simulations of the 30° wedge model with the calibration plate

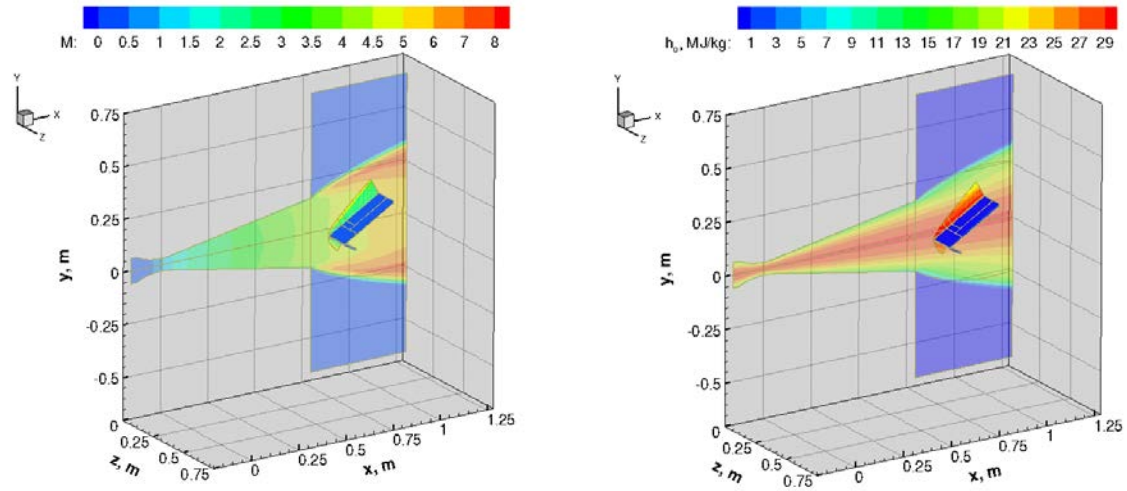

(a) Mach number **(b) total enthalpy**

Figure 10. Computed flowfield contours of the IHF 13-inch nozzle flow and test box with the 30° wedge model: $\dot{m}$ = 849 g/s, h_{ob} = 22.8 MJ/kg, h_{ocl} = 29.2 MJ/kg, parabolic enthalpy profile, 6.4% Ar, p_{box} = 2 torr.

Figure 10 shows the computed Mach number and total enthalpy contours of the IHF 13-inch nozzle flow downstream of the nozzle inlet. The contours are shown on the x-y symmetry planes of the nozzle flowfield and on other planes of interest for the flowfield of the test box and over the wedge model. For this case, the wedge model was tested at an off-centerline location (the leading edge of the wedge model is at 10.16 cm downstream of the nozzle exit and 3.81cm below centerline), thus reducing the effects of the expansion waves on the model surface quanties.

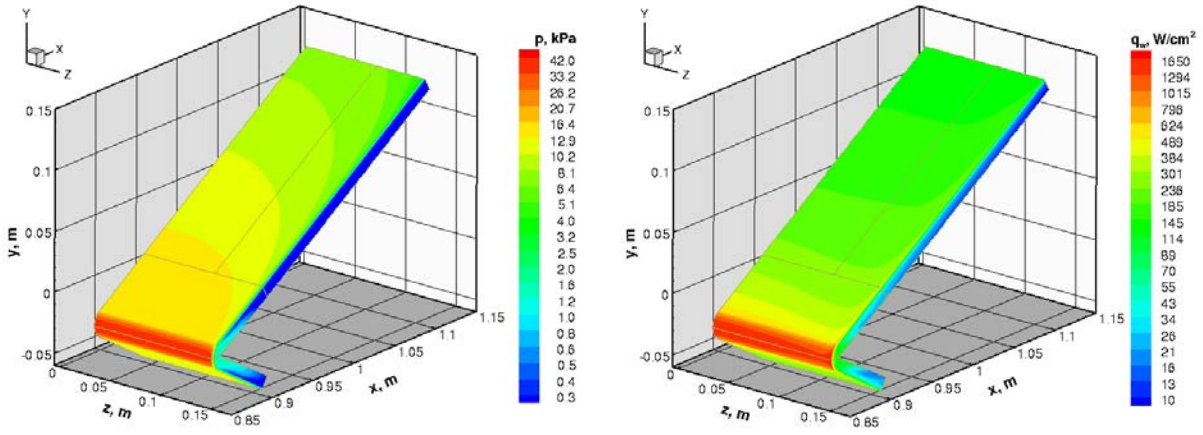

(a) pressure **(b) heat flux**

Figure 11. Computed surface quantities of the 30° wedge model with the water-cooled calibration plate. IHF 13-inch nozzle flow: $\dot{m}$ = 849 g/s, h_{ob} = 22.8 MJ/kg, h_{ocl} = 29.2 MJ/kg, 6.4% Ar.

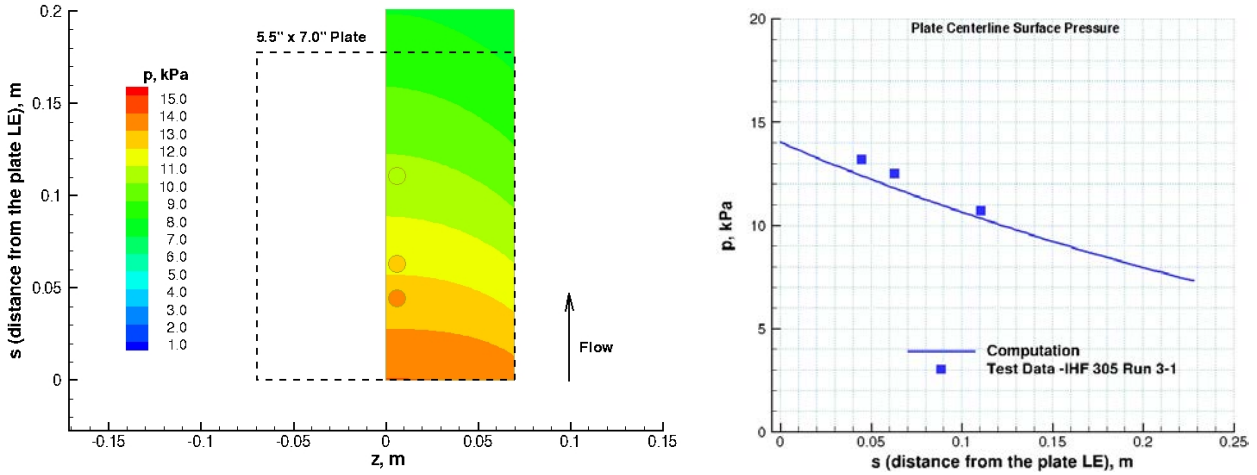

(a) pressure

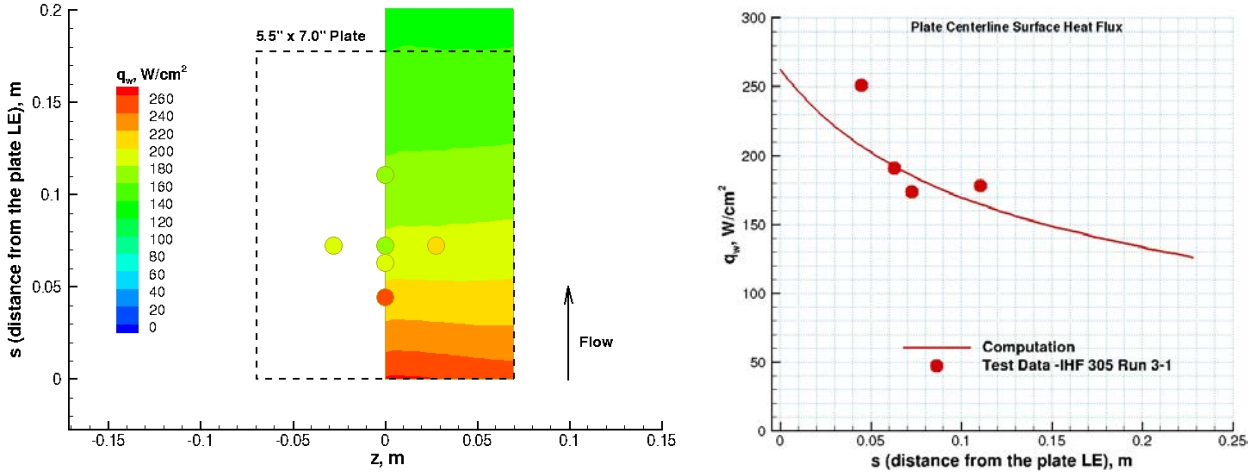

(b) heat flux

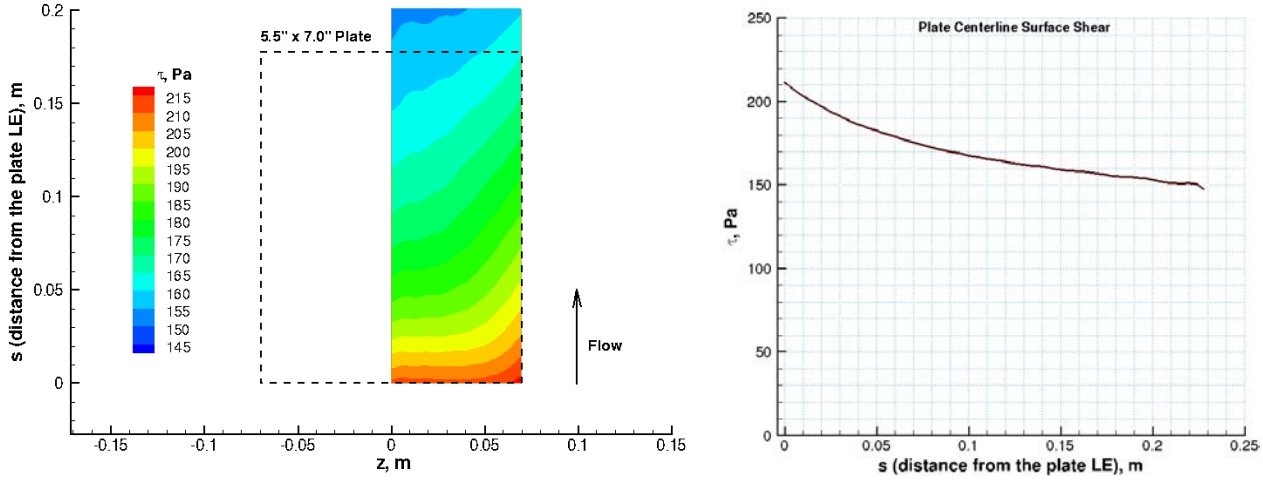

(c) shear

Figure 12. Computed surface quantities of the calibration plate using the 30° wedge model and comparisons with the calibration data. IHF 13-inch nozzle flow: $\dot{m}$ = 849 g/s, h_{ob} = 22.8 MJ/kg, h_{ocl} = 29.2 MJ/kg, 6.4% Ar. Symbols color-coded with the contour colors are the test data from IHF 305 Run 3-1.

Figure 11 shows contours of the computed surface quantities (pressure and heat flux) of the wedge model and the calibration plate. Note that the surface pressure decreases significantly along the wedge centerline, similar to the 20° wedge plate shown in Fig. 6a. However, here the pressure drop observed along the plate centerline is more gradual. This is primarily due to the three-dimensional conical flow expansion over the side of the model. Also, interaction of the expansion waves from the nozzle exit with the bow shock wave of the wedge model is somewhat limited. As mentioned, the effect of the expansion waves becomes more dominant when the model size and the nozzle exit diameter are comparable.

Figure 12 shows computed calibration-plate surface quantities and comparisons with the measured calibration plate data. Again, the contour plots show computed surface pressure and heat flux on one half of the calibration plate, and the symbols in the contour plots are the measurements, color coded with the same contour levels. Although the predicted surface pressures are in reasonably good agreement with the measurements, within ±5%, the slope of the predicted pressure drop appears to be slightly larger in the measurements, which may indicate that the location of the wedge model leading edge or wedge angle of attack might differ somewhat from those reported. Note that the calibration plate heat flux measurements show some asymmetry with respect to the plate centerline, although they are within the estimated uncertainty of the measurements, ±15%. Whether the source of this potential asymmetry is related to the heat flux gages Q_5 and Q_6 or the nozzle flowfield itself is not understood at this time. Also, note that Q_1 heat flux measurements, the first calorimeter on the centerline, is also substantially higher than the predictions. Overall, the agreement in the surface heat flux values is considered fair.

Table 2 gives a summary of the facility and calibration data obtained in IHF 305 tests, and corresponding CFD estimates. The tabulated values of surface pressure, heat flux (CWFC and HWFC), and shear are for the test plate centerline (not for the calibration plate). The wedge model in the test plate configuration includes an upstream copper plate (~3.1 cm). Note that CFD simulations of the wedge model with the smooth test plate for HWFC heat flux estimates are again not presented but the results are reported in Table 2.

Simulations of the 30° wedge model with the test plate

Similarly, CFD simulations of the 30° wedge model with the calibration plate and simulations of the wedge model with the test article are performed.

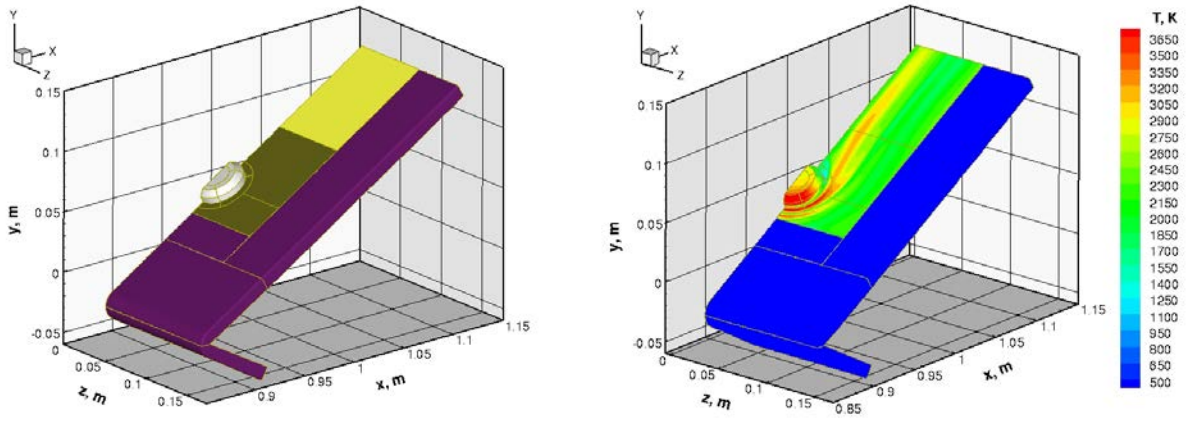

(a) 9.2-in wedge model geometry **(b) surface temperature**

Figure 13. Geometry of the 30° wedge model with the test plate and computed surface temperature contours. IHF 13-inch nozzle flow: $\dot{m}$ = 849 g/s, h_{ob} = 22.8 MJ/kg, h_{ocl} = 29.2 MJ/kg.

Figure 13 shows the geometry of the 30° wedge model with the test plate and computed surface temperature contours. Again, the water-cooled copper sections of the model are assumed to be at a constant temperature of 500 K while the test plate temperatures are computed using a radiative equilibrium boundary condition. The different colors on the wedge in Fig. 13a represent different materials: copper, compression-pad material, bolt, and heatshield material. Note that there is a copper plate in the wedge holder installed upstream of the test plate (~3.1 cm) in

Fig. 13a. Therefore, the leading edge of the test plate is about 3.1 cm downstream of the calibration plate leading edge shown in Fig 12.

Table 2. Summary of facility conditions, stagnation calorimeter and 30° wedge calibration plate data obtained in the IHF 13-inch nozzle at x_{ml} = 10.16 cm, and corresponding CFD estimated parameters.

	IHF 305 Tests Facility/Calibration Data		
	Run 3-1	**Run 4-1**	**Run 5-1**
p_{ch}, kPa	818	820	818
I, A	6012	5978	5994
V, V	6703	6722	6712
$\dot{m}$, g/s	849	849	849
$c_{Ar,\,\%}$	6.4	6.4	6.4
h_{ob} (W), MJ/kg	21.0	21.1	21.0
p_1, p_2, p_3, kPa	13.2, 12.5, 10.7	13.2, 12.6, 10.8	13.1, 12.5, N/A
Q_5, W/cm^2	184	183	189
Q_1, Q_2, Q_3, Q_4, W/cm^2	251, 191, 174, 178	257, 190, 173, 177	268, 192, 173, 175
Q_6, W/cm^2	205	204	196
q_{isoq}, W/cm^2	822	814	N/A
p_{isoq}, kPa	41.8	41.8	N/A
	CFD Estimates		
$\dot{m}$, g/s	849		
$c_{Ar,\,\%}$	6.4		
h_{ob}, MJ/kg	22.8		
$h_{ocl,}$ MJ/kg	29.2		
p_s, kPa	12.9 – 8.4		
q_s (CWFC), W/cm^2	221 – 139		
q_s (HWFC), W/cm^2	165 – 127		
τ_s, Pa	191 – 155		
δ, cm	0.49		
M_e	1.62		
Re_x	8.6x10^3		

Note that CFD-estimated surface quantities are given as a range from the test plate leading edge to 15.4 cm downstream (not including the upstream copper section), and estimates for δ and M_e are given at the test plate leading edge location.

Figure 14 shows contours of the computed surface pressure, heat flux and shear stress on one half of the test plate with the bolt, and the corresponding profiles along the plate centerline. Again, in order to make interpretation of the centerline profiles easier, the geometry of the test plate is also shown. For this case, the copper section upstream of the test plate is included because the separated flow or flow disturbance region extends upstream of the test plate leading edge. On the line plots, the dashed line represents the water-cooled copper plate surface upstream of the test plate. Although these results are somewhat similar to those presented in Fig. 9, there are some significant differences. For this case, the total protuberance height is much larger (~1 cm vs 0.4 cm), and the ratio of the step height to the boundary layer thickness is larger (~2 vs 1.5); the bolt diameter is smaller (~4.1 cm vs 5.2 cm); the boundary layer edge Mach numbers are similar (~1.62 vs 1.56); and the pressure gradients on the smooth surface plate are much lower (Fig. 7a vs Fig. 12a). As a result, the extent of the flow disturbances by the bolt is larger. As in

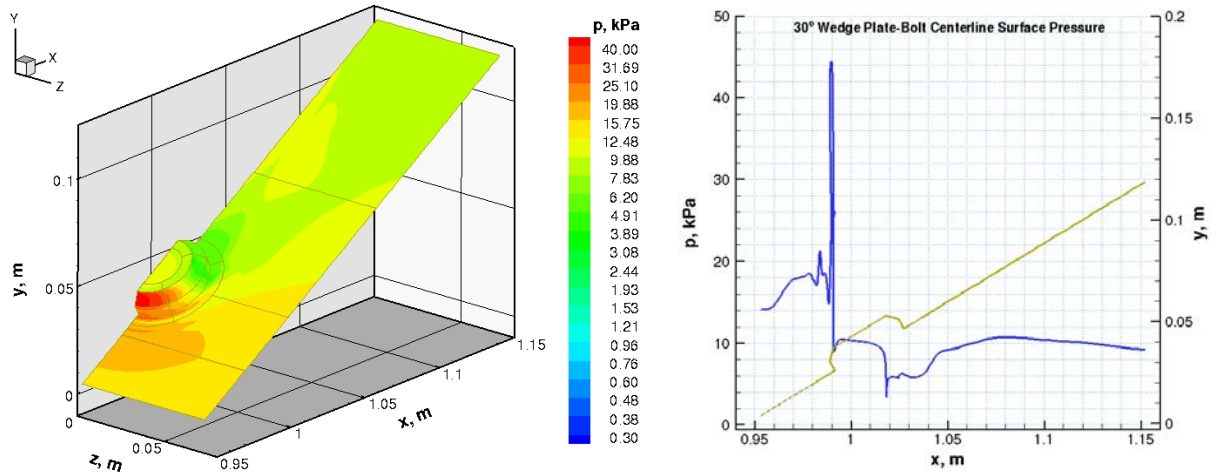

(a) pressure

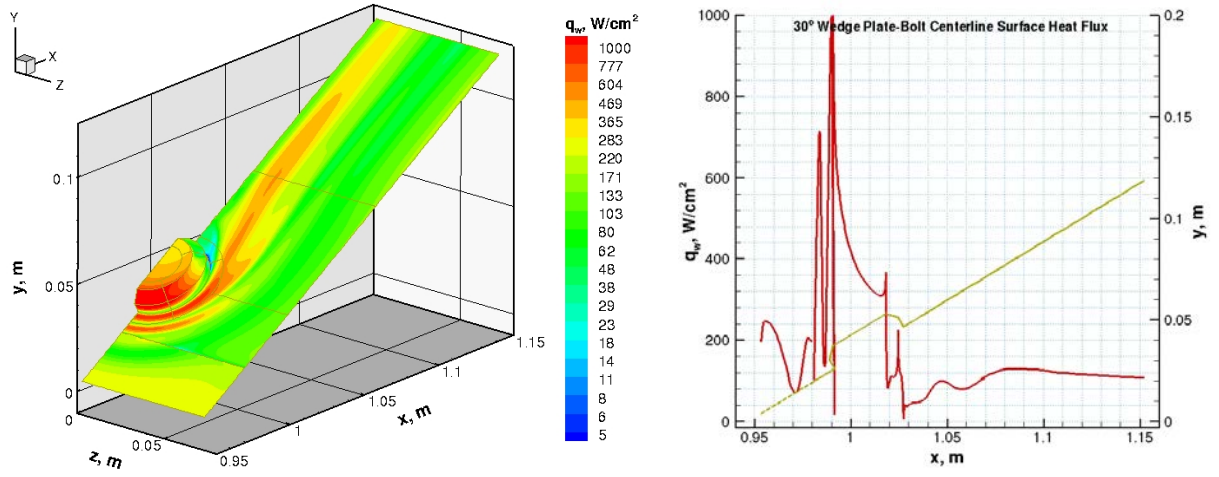

(b) heat flux

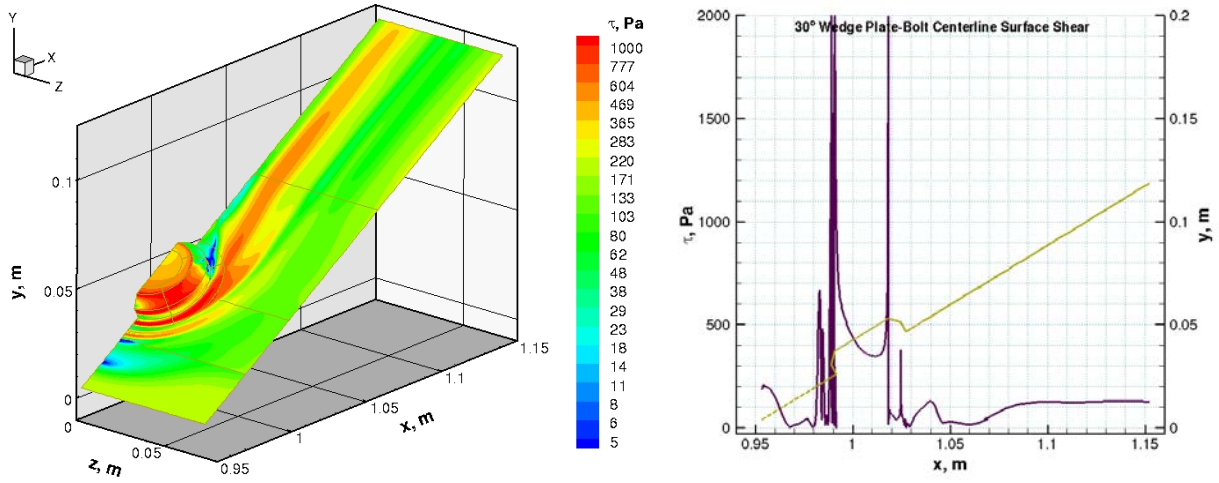

(c) shear

Figure 14. Computed surface quantities of the test plate using the 30° wedge model. IHF 13-inch nozzle flow: $\dot{m}$ = 849 g/s, h_{ob} = 22.8 MJ/kg, h_{ocl} = 29.2 MJ/kg.

the 20° wedge model, two primary augmented heating regions upstream of the bolt and around the bolt are also predicted by CFD simulations. However, an additional augmented heating region upstream of the test plate on the copper section (although not as prominent as the other two), is also predicted, as shown in Fig. 14b. The computed surface shear stress contours shown in Fig. 14c clearly demonstrate stagnant and separated regions in the flowfield, as these regions exhibit relatively low shear levels.

D. Discussion of Protuberance Induced Flowfield Features

Many factors potentially affect flow field structure over a flat plate with a circular protuberance in a supersonic flow: boundary layer thickness, protuberance diameter, step height and its geometry, edge Mach number, Reynolds number, pressure gradient over the plate, etc. There are several classifications of these protuberances in the literature,[16-18] depending on whether the protuberance affects the external flow or not. When the protuberance height is much less than the boundary-layer thickness, then it is considered to be a small disturbance. For small disturbances, resulting flow features are described in terms of vortex systems (e.g., horseshoe vortex), and flow separation and viscous and inviscid flow interactions are not as prominent. When the protuberance height is not much less than the boundary-layer thickness, they are considered to be either intermediate or large protuberances. For the two wedge tests analyzed in the paper, total protuberance heights are greater than the estimated boundary layer thicknesses (~0.38 cm total step height in 0.25-cm thick boundary layer for IHF 309 tests, and ~1 cm total step height in 0.5-cm boundary layer for IHF 305 tests). For these cases, the boundary layer upstream of the protuberance separates, and this separation results in a strong interaction between the viscous and inviscid flow features, shock-boundary layer and shock-shock interactions. The other limiting condition, when the protuberance height is much larger than the boundary layer thickness, is considered to be a cylindrical protuberance or obstacle (e.g., interaction of bow shock of a blunt fin with the boundary layer).

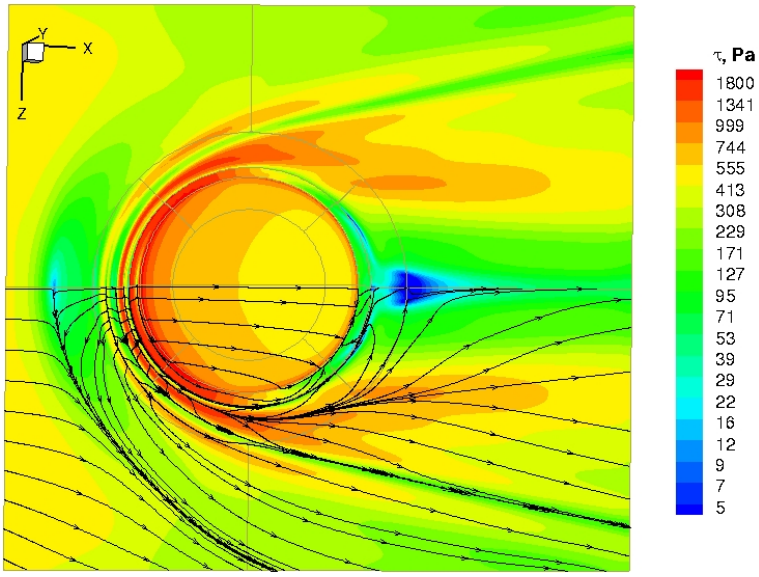

Figure 15. Computed surface shear contours of the 20° wedge test plate with surfaces streamlines (full plate, top view). IHF 6-inch nozzle flow: $\dot{m}$ = 849 g/s, h_{ob} = 21.5 MJ/kg, h_{ocl} = 29.2 MJ/kg, 6.4% Ar.

As mentioned earlier, surface shear contours are very informative to map out important flow features. Figure 15 shows the computed shear contours on the 20° wedge test plate. This is a top view of the plate shown in Fig. 9c, showing the separated and attached flow regions near the surface. Starting from the plate leading edge, the flow on the centerline goes through a separation first and then it reattaches, subsequently separates and reattaches again until it stagnates at the bolt leading edge. Whenever there is a flow reattachment, it is manifested by increased shear values (much higher than those of the upstream attached flow). Also, as shown earlier in Figs. 9 and 14, the higher shear regions correspond to higher heating levels. These features are convected downstream on both sides of the bolt similar to a horseshoe vortex pattern. This flow structure is the result of complex interaction between the bow shock formed by the bolt protrusion and the approaching supersonic boundary layer.

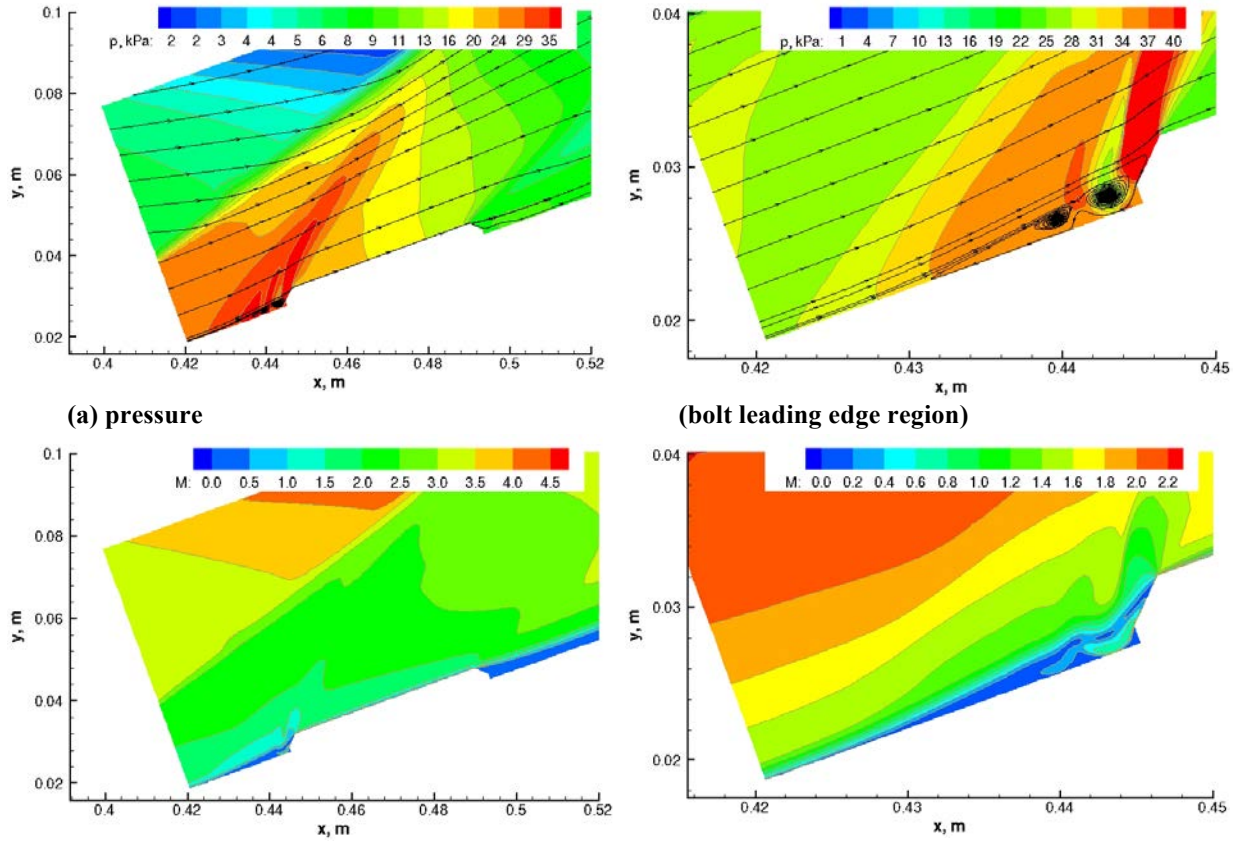

(a) pressure **(bolt leading edge region)**

(b) Mach number **(bolt leading edge region)**

Figure 16. Computed pressure and Mach number contours near the bolt region on the 20° wedge model. IHF 6-inch nozzle flow: $\dot{m}$ = 849 g/s, h_{ob} = 21.5 MJ/kg, h_{ocl} = 29.2 MJ/kg, 6.4% Ar.

In order to clarify the predicted flowfield around the bolt, computed flowfield contours on the symmetry plane are presented in Fig. 16. As noted, the flowfield around the bolt is complex and three-dimensional. Due to the bolt protrusion, the flowfield upstream of the bolt is separated, and two primary shock waves are formed. A primary separation bubble is formed at the leading edge of the bolt. The first shock wave originates at the upstream edge of this bubble. As a result of shock-wave boundary layer interaction, the flow separation region extends further upstream, and another shock wave is formed at the reattachment point. As the flow passes the protuberance, there are expansion waves at the trailing edge, and a large separated flow region is generated.

These two separated flow regions and subsequent reattachments shown here on the centerline remain intact as the flow goes around and passes the bolt and they are convected downstream along the test plate, as can be inferred from the surface streamlines in Fig. 15. It should be mentioned that for this case, interaction of the shock waves formed from the bolt protrusion with the bow shock of the wedge model is minimal. If the bolt height is increased, this interaction becomes more important. In fact, as part of the feasibility study for the IHF 6-inch nozzle wedge tests, pretest CFD simulations were performed to evaluate this concern (shock formation from the bolt protrusion and its interaction with the wedge shock wave), and they provided guidance for the test article design (specifically, on the bolt height, diameter, and its location on the wedge plate). Some of the results from these simulations, showing the interaction of the primary bolt shock with the bow shock of the wedge model, are given in the Appendix.

Figure 17 shows the predicted flowfield around the bolt, computed flowfield contours on the symmetry plane for the IHF 13-inch nozzle 30° wedge tests. For this case, the protuberance height is bigger, and the extent of flow separation and its flow interactions is larger. In addition to the two separated regions upstream of the bolt observed in the 20° wedge tests shown in Fig. 16, another separated region, a third one, is formed upstream of the bolt,

although it is much smaller than the other two. Aside from the protuberance height, the pressure gradient over the test plate is likely to be a factor for the flow separation. A favorable pressure gradient is known to delay the flow separation. In this case, the pressure gradients on the smooth surface plate are much lower (Fig. 7a vs Fig. 12a).

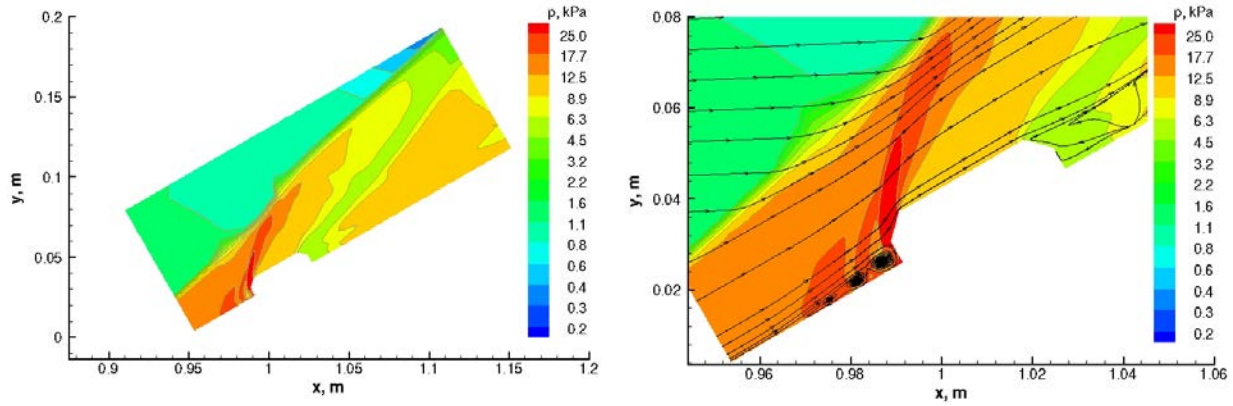

(a) pressure

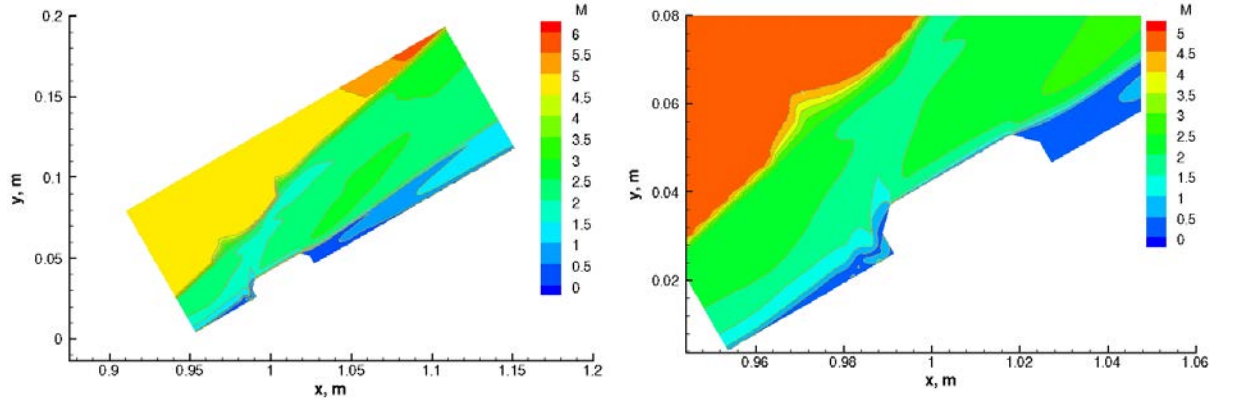

(b) Mach number

Figure 17. Computed pressure and Mach number contours near the bolt region on the 30° wedge model. IHF 13-inch nozzle flow: $\dot{m}$ = 849 g/s, h_{ob} = 22.8 MJ/kg, h_{ocl} = 29.2 MJ/kg, 6.4% Ar.

E. Comparisons of Qualitative Heating Patterns

Although comparisons of the smooth surface CFD wedge simulations with the calibration plate data provide some validation, the CFD simulations of the wedges with the test articles lack similar direct comparisons with the test data. Especially when the flowfield is very complex, as described in the previous sections, it is fair to question the validity of these predicted heating patterns on the test plate with the bolt. Therefore, at this point, it is useful to show images of heating patterns observed during the tests and make qualitative comparisons with CFD predictions. During both IHF 309 and IHF 305 tests, the test articles were viewed with a HD video camera and an IR camera from the top. HD video footage and IR temperature maps of the wedge test plates are provided from the test facility as qualitative data, from which a few frames have been selected.

Figure 18 presents HD and IR images of the 20° wedge test article. These images, taken right before the separation bolt started to melt and soon afterwards, provide qualitative heating distributions on the test article. Both images clearly show the separation and reattachment lines upstream of the bolt and its sides. The dark regions on the test plate represent relatively cold separated flow regions. CFD-predicted surface temperature contours are also presented in Fig. 18c, showing qualitatively similar distributions. Note that the view angle for CFD contours is perpendicular to the plate surface but the view angles for the HD and IR images are not exactly perpendicular to the plate. It is also interesting that the graphite conditioning plate does not appear to be hot in the HD image in Fig. 18a. This is because the graphite plate has not reached equilibrium temperature yet. (Other HD images taken later in time show that the graphite plate is heated and the bolt is melting, not shown here.)

(a) HD camera image, IHF 309 Run 3

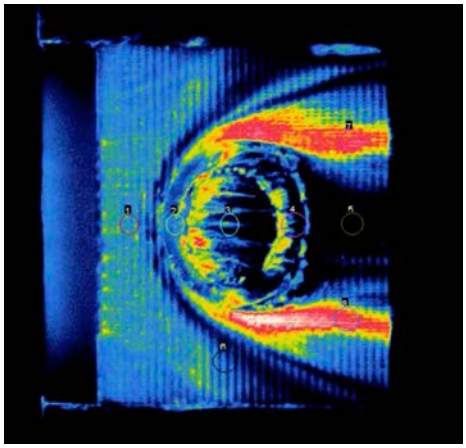

(b) IR camera image, IHF 309 Run 2

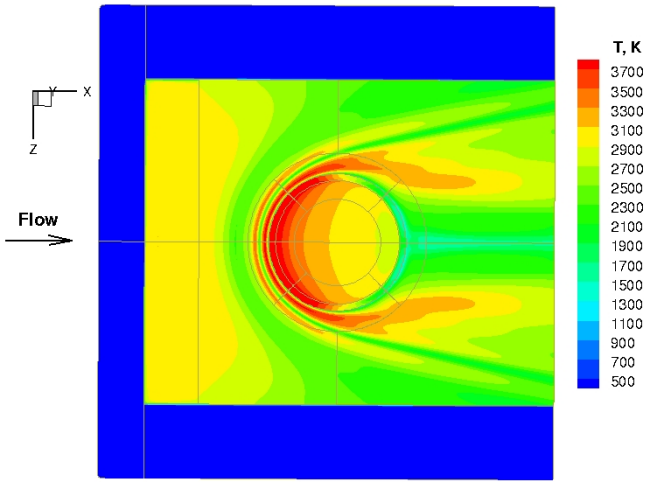

(c) CFD simulation, surface temperature (top view)

Figure 18. Qualitative heating patterns observed from the HD and IR cameras, and CFD simulation. The 20° wedge model in the IHF 6-inch nozzle flow, IHF 309 tests.

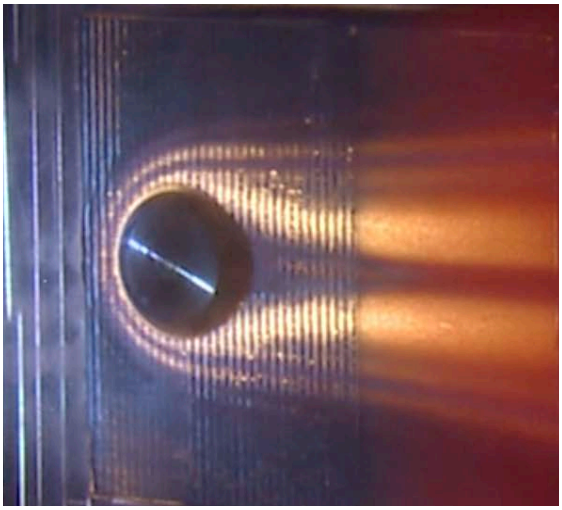

(a) HD camera image

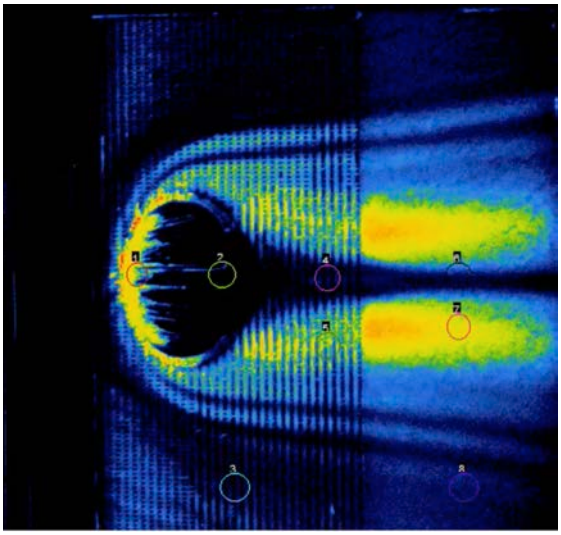

(b) IR camera image

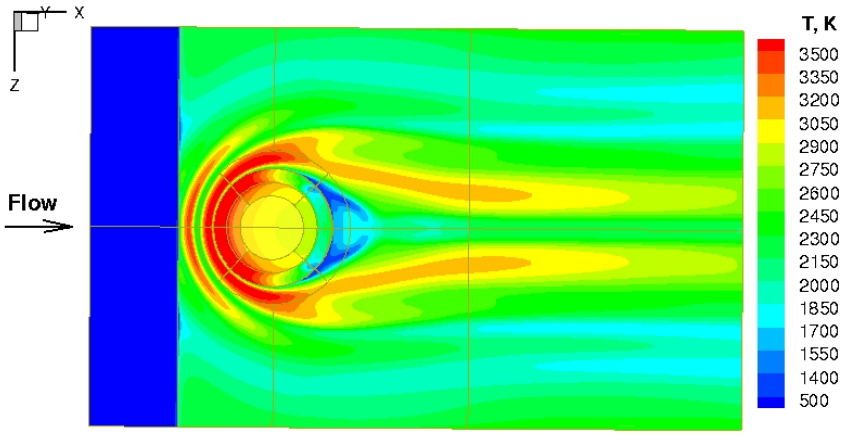

(c) CFD simulation, surface temperature (top view)

Figure 19. Qualitative heating patterns observed from the HD and IR cameras, and CFD simulation. The 30° wedge model in the IHF 13-inch nozzle flow, IHF 305 Run 5.

Figure 19 presents HD and IR images of the 30° wedge test article, and CFD-predicted surface temperatures. These images, again similarly taken right before the separation bolt started to melt and sometime after, show that not only are there two primary augmented heating regions upstream of the bolt and around the bolt, but also a third one (cold and hot regions, or separated flow followed by reattachment). Most of these features are well predicted by CFD simulations.

F. Computational Grid Details and Estimated Uncertainties

The two-dimensional axisymmetric and three-dimensional CFD computations of the IHF 6-inch and 13-inch nozzle flowfields, including the test box and models, were performed using multi-block grids. All computational grids were generated using a commercial software package, *Gridgen*.[19] For the axisymmeric IHF 6-inch and 13-inch nozzle simulations with stagnation models, 1.056×10^5 and 1.152×10^5 cells were used respectively; the number of cells from the nozzle inlet to the nozzle exit was 360 for the 6-inch nozzle and 480 for the13-inch nozzle, with 120 cells normal to the wall along the nozzle. For the three-dimensional IHF 6-inch and 13-inch nozzle/test box flowfields, 12.31 and 13.93 million cells were used, respectively. For the 20° and 30° wedge models with the calibration plates, the grid sizes were 3.17 and 3.89 million cells; and for the corresponding test plates with the bolt, the grids (for test plate only) had 3.02 and 3.67 million cells. Based on a limited number of grid refinement studies, the grid quality issues of the computations and numerical accuracy were adequately addressed.

However, CFD computations of arc-jet flows, as for hypersonic flight simulations, include uncertainties in many of the model input parameters. It is not possible at this time to do a complete uncertainty analysis of computed results for all of the simulation input parameters. The most important input parameter of the arc-jet test flow is the total enthalpy distribution at the nozzle inlet. Noting that the centerline total enthalpy used in CFD simulations rely on calorimeter data, calibration plate measurements, facility data, and other modeling input parameters; the uncertainty in the heat flux predictions for the wedge calibration plates is estimated to be as much as ±20%, and the uncertainty in the surface pressure predictions is estimated to be ±5-10%. For the test article with the bolt, uncertainties in predicted surface pressure, heat flux, and shear and their distributions are clearly larger. Although qualitative comparisons presented in Section D are very encouraging, these uncertainties cannot be assessed without further validation tests with varying bolt heights and geometries.

V. Summary and Concluding Remarks

Computational simulations in support of two arc-jet tests in the NASA Ames 60-MW Interaction Heating Facility flow are presented. These tests were conducted using two different wedge models, each placed in a free jet downstream of a corresponding different conical nozzle: one in the IHF 6-inch nozzle, and other in the IHF 13-inch nozzle. Panel test articles included a metallic separation bolt imbedded in the compression-pad and heatshield materials, resulting in a circular protuberance over a flat plate. The calibration test data included heat flux and pressure measurements with stagnation calorimeters, and measurements of surface pressure and heat flux on calibration plates integrated with two wedge models.

For each test configuration, computations of the nonequilibrium flowfield in the nozzle, test box, and over the test articles are performed. These simulations take into account nonuniformities in the total enthalpy and mass flux profiles at the nozzle inlet as well as the expansion waves emanating from the nozzle exit and their effects on the model flowfields, and they predict model surface pressure and heat flux measurements consistent with the set of arc-jet facility data. For the test articles with the separation bolt, CFD simulation is the only reliable tool to provide heating and pressure distributions needed for material thermal response simulations. Predicted heating distributions on the test articles including the compression-pad separation bolt are qualitatively in good agreement with images from HD and infrared cameras. Both camera images and computations show that the surface heating distributions of the test articles have multiple augmented heating regions due to complex flow interactions such as shock-shock and shock-boundary layer interactions.

Since the arc-jet flowfield over the compression-pad separation-bolt test article is complex, traceability of the arc-jet test environment to the flight environment can only be achieved through validated computational tools. As demonstrated in earlier work for other Ames arc-jet facilities, CFD simulations of the IHF flow can assist test

planning, define arc-jet test environments for surface properties of TPS, reduce exploratory testing, and provide a framework for tracing the TPS performance from this ground test facility to flight.

Acknowledgments

This work was funded by the NASA Orion TPS Insight/Oversight project. The arc-jet operational capability at NASA ARC is also supported by NASA-SCAP. The authors would like to thank Eric I. Esposito of Lockheed Martin Space Systems for the compression-pad/separation bolt test article designs, and all of the facilities staff involved in the IHF tests, in particular, test engineers Frank C. L. Hui and Imelda Terrazas-Salinas. The support from the NASA Ames Entry Systems and Technology Division, through contract NNA15BB15C to AMA, Inc., is gratefully acknowledged.

References

[1]Terrazas-Salinas, I., and the staff of Thermophysics Facilities Branch, "Test Planning Guide for NASA Ames Research Center Arc-Jet Complex and Range Complex," A029-9701-XM3 Rev. C, Entry Systems and Technology Division, NASA Ames Research Center, April 2009.

[2]Thompson, R. A., Lessard, V., Jentink, T., and Zoby, E. V. "Analysis of Compression Pad Cavities for the Orion Heatshield," AIAA Paper 2009-1575, Jan. 2009.

[3]Hollis, B. R., "Compression Pad Cavity Heating Augmentation on Orion Heat Shield," *Journal of Thermophysics and Heat Transfer*, Vol. 25, No. 3, 2011, pp. 329-340; also AIAA Paper 2009-3843, June 2009.

[4]Fretter, E., "Interaction Heating Facility (IHF) Fact Sheet," http://www.nasa.gov/centers/ames/thermophysics-facilities-home, Thermophysics Facilities Branch, Entry Systems and Technology Division, NASA Ames Research Center, Sept. 2016.

[5]Smith, M. D., Moody, H., Wanstall, C., and Terrazas-Salinas, I., "The Design and Use of Calorimeters for Characterization of High-Enthalpy Flows in Arc-Heated Test Facilities," AIAA Paper 2002-5236, Sept. 2002.

[6]Driver, D. M., Hui, F., Gökçen, T., Raiche, G. A., Balboni, J. A., Terrazas-Salinas, I., Mayeaux, B., Lin, F., and Lester, D., "Aeroheating Testing Approach for Shuttle Wing Leading Edge Repair Concepts," AIAA Paper 2006-3297, June 2006.

[7]Wright, M. J., Candler, G. V., and Bose, D., "Data-Parallel Line Relaxation Method for the Navier-Stokes Equations," *AIAA Journal*, Vol. 36, No. 9, 1998, pp. 1603-1609.

[8]Wright, M. J., "Data-Parallel Line Relaxation Code, DPLR Version 4.02," Private Communication, June 2010.

[9]Park, C., *Nonequilibrium Hypersonic Aerothermodynamics*, John Wiley & Sons, Inc., New York, 1990, Chap. 4.

[10]Gökçen, T., Skokova, K., Balboni, J. A., Terrazas-Salinas, I., and Bose, D., "Computational Analysis of Arc-Jet Wedge Calibration Tests in IHF 6-Inch Conical Nozzle," AIAA Paper 2009-1348, Jan. 2009.

[11]Gökçen, T., Chen, Y. K., Skokova, K. A., and Milos, F. S., "Computational Analysis of Arc-Jet Stagnation Tests Including Ablation and Shape Change," *Journal of Thermophysics and Heat Transfer*, Vol. 24, No. 4, 2010, pp. 694-707; also AIAA Paper 2009-3596, June 2009.

[12]Gökçen, T., Balboni, J. A., and Alunni, A. I. "Computational Simulations of the 10-MW TP3 Arc-Jet Facility," AIAA Paper 2015-3103, June 2015.

[13]Gökçen, T., and Alunni, A. I. "Flow Characterization Studies of the 10-MW TP3 Arc-Jet Facility: Probe Sweeps," AIAA Paper 2016-4153, June 2016.

[14]ASTM E637-05, "Standard Test Method for Calculation of Stagnation Enthalpy from Heat Transfer Theory and Experimental Measurements of Stagnation-Point Heat Transfer and Pressure," American Society for Testing and Materials, November 2005 (originally published in 1978).

[15]Winovich,W., "On the Equilibrium Sonic-Flow Method for Evaluating Electric-Arc Air-Heater Performance," NASA TN-D-2132, March 1964.

[16]Korkegi., R. H., "Survey of Viscous Interactions Associated with High Mach Number Flight," *AIAA Journal*, Vol. 9, No. 5, April 1971, pp. 771-784; also AIAA Paper 70-781, June 1970.

[17]Sedney, R., "A Survey of the Effects of Small Protuberances on Boundary-Layer Flows," *AIAA Journal*, Vol. 11, No. 6, June 1973, pp. 782-792; also AIAA Paper 72-713, June 1972.

[18]Sedney, R., and Kitchens Jr., C. W., "Separation ahead of Protuberances in Supersonic Turbulent Boundary Layers," *AIAA Journal*, Vol. 15, No. 4, April 1977, pp. 546-552; also AIAA Paper 76-163, Jan. 1976.

[19] "Gridgen, Version 15.17," Pointwise, Inc., Fort Worth, TX.

Appendix: Pretest simulation results, showing shock formation from the bolt protrusion and its interaction with the wedge shock wave (Figs. A1-A2)

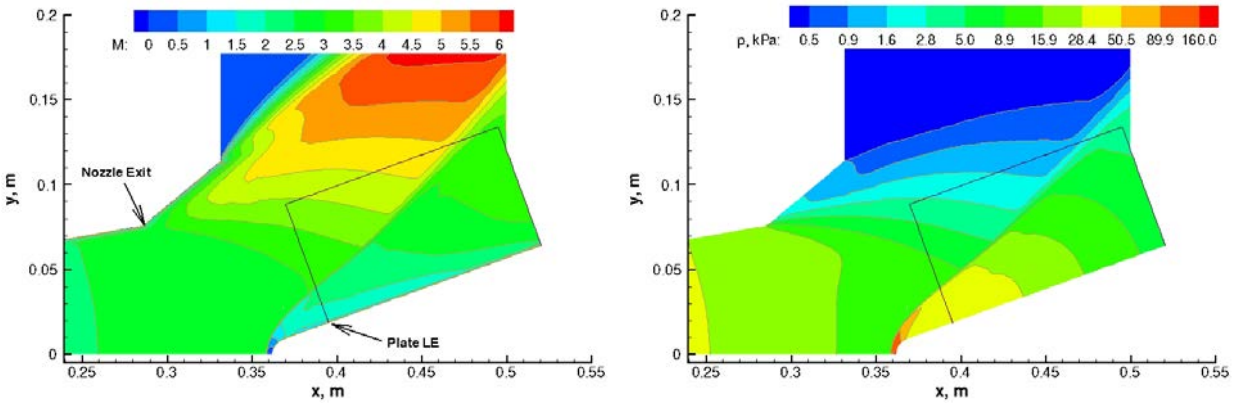

(a) Mach number **(b) pressure**

Figure A1. Computed flowfield contours near the IHF 6-inch nozzle exit, including test box with the 20° wedge model at x_{ml} = 7.62 cm (on symmetry plane). Pretest calculations, p_o = 894 kPa, $h_{ob} = h_{ocl}$ = 26.3 MJ/kg, 6.4% Ar.

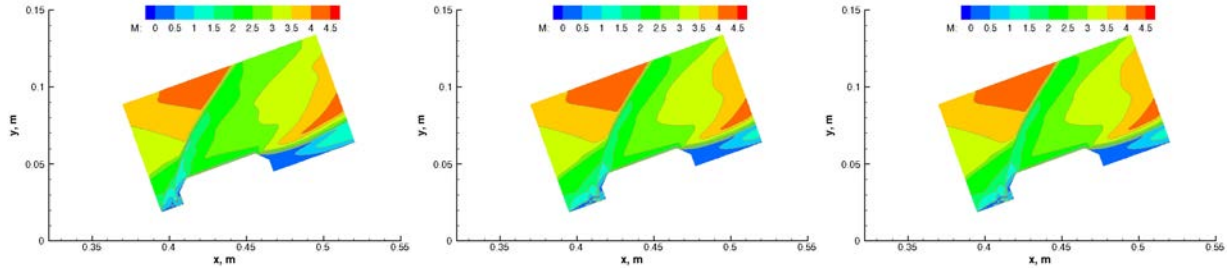

(a) h_{bolt} = 1.54 cm, h_{step1} = 0.82 cm, 45° bevel angle

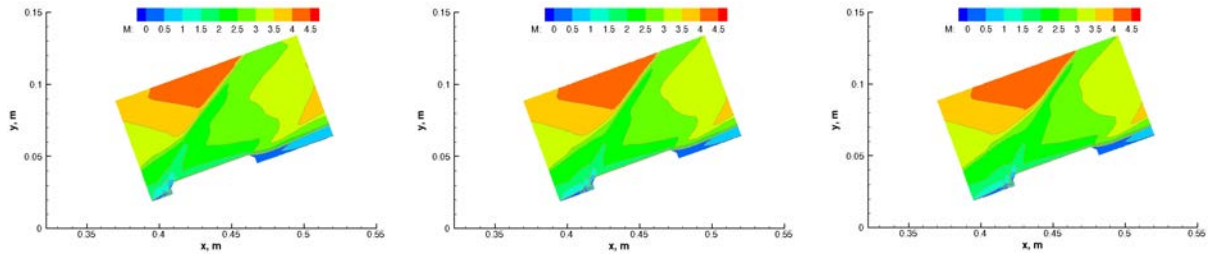

(b) h_{bolt} = 0.77 cm, h_{step1} = 0.41 cm, 45° bevel angle

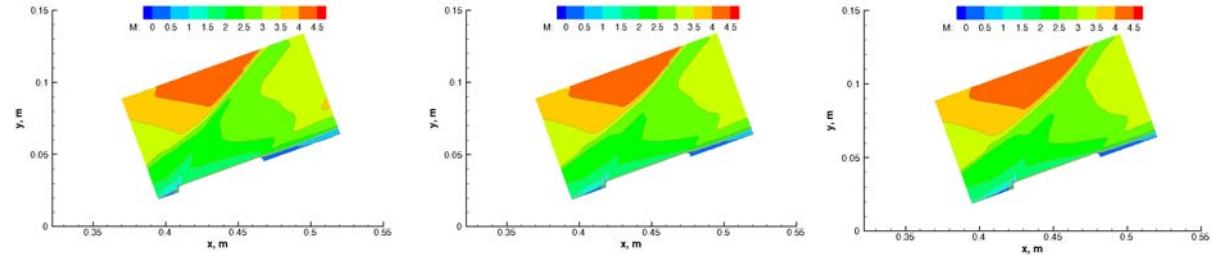

(c) h_{bolt} = 0.38 cm, h_{step1} = 0.21 cm, 45° bevel angle

Figure A2. Computed Mach number contours near the bolt region of the test plate using the 20° wedge model at three bolt locations (~1.52 cm, 2.54 cm, and 3.05 cm from the plate leading edge) for three bolt heights. D_{bolt} = 6.19 cm. IHF 6-inch nozzle flow: p_o = 894 kPa, $h_{ob} = h_{ocl}$ = 26.3 MJ/kg, 6.4% Ar.